Received: 22 October 2023 | Revised: 25 February 2024 | Accepted: 21 March 2024

DOI: 10.1002/nag.3733

RESEARCH ARTICLE

WILEY

Stochastic assessment of 3-D tunnels in near-fault ground motion using modified domain reduction method

Bhavesh Banjare[1] | **Gauri Ranjan Krishna Chand Avatar**[2]

[1]Department of Civil Engineering, Indian Institute of Science, Bengaluru, India

[2]Department of Aerospace Engineering, Indian Institute of Science, Bengaluru, India

Correspondence
Bhavesh Banjare, Department of Civil Engineering, Indian Institute of Science, Bengaluru, India.
Email: bhaveshb@iisc.ac.in

Abstract

A robust assessment of tunnels due to uncertainties present in soil and ground motion properties can affect the dynamic response of these structures. In this paper, a stochastic analysis considering an aleatory variability in shear velocity V_S by performing Monte Carlo simulations and assessing its influence on underground tunnels. To numerically assess the response of the soil-tunnel system to near-fault earthquake ground motion, the required computational domain usually spans multiple kilometers including both earthquake fault and the structure. Thus, these simulations are computationally expensive. An efficient alternative method, that is, the Domain Reduction Method (DRM), in which a modular two-step methodology for reducing the computational costs in the large domain analysis is employed. A 3-D soil-tunnel structure interaction is modeled to simulate the response of tunnel subjected to an inclined earthquake fault. The numerical simulation of the soil-tunnel-fault system is conducted in an open-source FE package called Multi-hazard Analysis for STOchastic time DOmaiN phenomena (MASTODON) based on MOOSE framework. The interactive analyses are carried out for three distinct types of soils based on National Earthquake Hazards Reduction Program (NEHRP) provision, that is, soft, medium, and hard, by generating 130 realizations. The results provide many insights into the influence of local site effects, that is, frequency shift for the peak response and the importance of input ground motion characteristics that govern the response of underground structures. The dynamic response of the structure is very sensitive to the uncertainty in rock material properties, especially, the stiffness of the rock sample and the shear wave velocity.

KEYWORDS

domain reduction method, dynamic soil-structure interaction, inclined seismic wave propagation, stochastic analysis, tunnels

1 | INTRODUCTION

The development of underground tunnels has received significant attention due to its being an integral part of the infrastructure of developed cities worldwide. These underground structures lie at shallow depths and pass through different soil zones. Projects involving tunneling through soft soil require rigorous consideration of all possible loading

 © 2024 John Wiley & Sons Ltd.

scenarios to mitigate damage. Among all the considerations, minimizing damage due to seismic loading is the most crucial aspect. Numerous instances of tunnel failure due to earthquakes have been seen in seismically active regions, such as in China, Japan, Italy, Taiwan, U.S., and Mexico. Recent earthquake events (Kobe earthquake 1995, Chi-Chi earthquake 1999, Wenchuan earthquake 2008, Tohoku earthquake 2011) have proven the vulnerability of underground structures to these earthquakes.[1–3] Owen and Scholl[4] described tunnel deformation modes, such as racking and ovaling, axial deformation, and curvature deformation. Hashash et al.[5,6] proposed a three-step method to quantify seismic hazards and estimate earthquake magnitude at the site. Penzein[7] produced closed-form analytical solutions to evaluate the response of tunnel lining in terms of thrust and bending moment and deformation modes. Some literature emphasizes that the ultimate bearing capacity of the soil domain would be affected by the soil spatial variability and ground motion characteristics.[8–11] Mollon et al.[12,13] considered a 2D limit analysis mechanism to study the effect of arbitrary friction angle and shear strength parameters on the breakdown pressure of tunnel faces. Chong et al.[14] explored random field theory to evaluate the collapse load of soil-tunnel systems in spatially variable sands. Using Monte Carlo simulations, Eshraghi and Zare[15] examined the tunnel face stability. Researchers[12–15] worked on finding the face stability of lined tunnels, while the stability of unlined tunnels was not considered for analysis.

Modeling earthquake ground motion of a fault with heterogeneous topography usually requires a large computational domain to simulate an infinite soil domain. In finite element analysis, to achieve robustness, accuracy, and efficiency, the spatial and temporal discretization needs to satisfy the stability criteria (i.e., the maximum grid size of the model is proportional to the lowest shear wave velocity and, inversely proportional to the highest relevant frequency of interest) of wave propagation in finite medium proposed by Ihlenburg and Babuska.[16] The computational domain needs to be discretized into many elements and nodes for simulating seismic wave propagation, due to which 3D soil-structure interaction models still require incredibly high processing time, despite advancements in computational tools for ground motion simulation.

One of the valuable features in seismic analysis of tunnel-fault-soil systems is proper modeling of the infinite soil domain. The infinite soil domain should be truncated by considering artificial absorbing boundaries at the edge of the semi-infinite domain. This artificial boundary is used for absorbing the scattered waves generated from the free surface and structures on the interaction of waves. Researchers have proposed several types of artificial boundaries over a few decades.[17–23]

Proper modeling of input ground motion for the soil-structure system requires an in-depth understanding and accurate modeling of fault rupture mechanism, propagation path of earthquake waves, local site effects, and soil-structure interaction. Depending on the chosen scenario, each factor can influence the input ground motion and the structural response. Researchers[24–26] have done noteworthy studies in earthquake modeling in recent years.

Numerical modeling requires two different scale measures for the tunnel-soil-fault system. Usually, a fault is spanned by multiple kilometers (seismological scale) and localized regions of interest, that is, tunnel-soil system scales are in meters (engineering scale). Both scenarios must be appropriately combined to get more accurate and logical results. There are two methods to approach these issues, that is, direct and hybrid methods. In the direct method, all the problem components are modeled in one system, that is, the fault rupture mechanism and its interaction with the structure. This approach is time-consuming and less efficient as we consider the large dimension of the fault rupture model and wave propagation path (usually several kilometers). The hybrid method divides the problem into two steps, leading to an efficient and accurate approach with lower computational costs. In the first step, we consider a free-field scenario, that is, only computation of ground motion in the domain and no structure interaction. In the second step, we consider smaller domains with structure and incorporate the nodal forces computed from the first step. Mossessian and Dravinski[27] used a hybrid method (i.e., boundary integral equation approach with finite element method) to examine the diffraction of plane P, SV, and Rayleigh waves due to subsurface irregularities of dipping layers of random shapes. Fäh et al.[28] generated ground motion of the Michoacan earthquake in 1985 in the 2D heterogeneous anelastic medium using the hybrid technique (i.e., modal summation with finite element method). Bielak et al.[29] developed a mixed variational formulation (i.e., BEM-FEM) to examine the soil amplification in inhomogeneous alluvial valleys due to inclined SH waves.

Domain reduction method (DRM) developed by Bielak et al.[30] is a two-step finite element methodology for seismic ground motion modeling of large-scale problems, including the source (i.e., fault rupture), wave propagation path, and locally complex geological and structure effects. Yoshimura et al.[31] verified the DRM using green's function algorithm. They also illustrated the application of the DRM to 3-D problems, including external sources (i.e., fault), and can be used for modeling all seismic waves (i.e., body waves: SV, SH, and P-waves; surface waves: Rayleigh and Love waves). DRM method accuracy was examined using two non-reflecting boundaries: the cone boundary[32] and the viscous boundary. The cone boundary was slightly better than the viscous boundary.[33] DRM method was further extended by Kontoe et al.[34] for modeling dynamics problems of consolidation. This algorithm significantly reduced the computational cost and increased

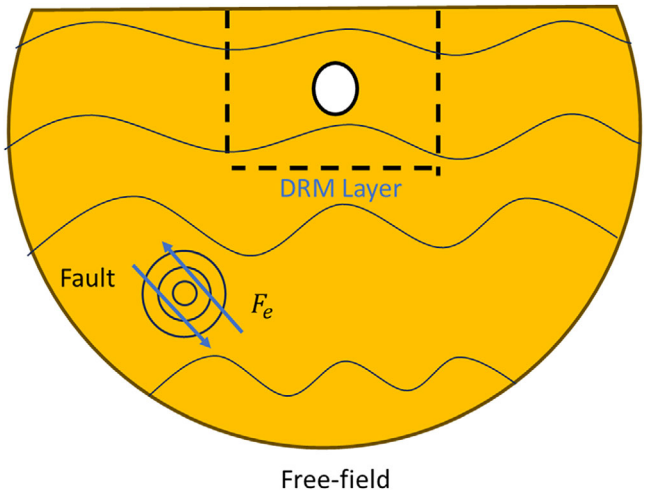


FIGURE 1 Schematic of tunnel-fault-soil system.

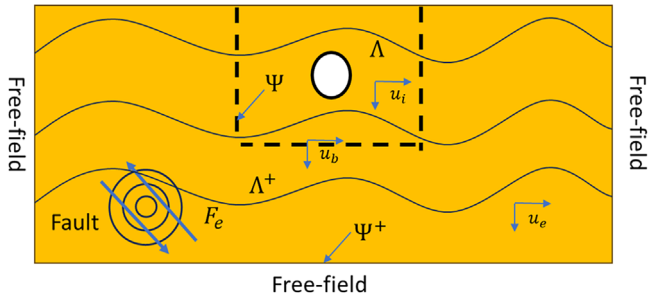


FIGURE 2 Schematic of semi-infinite seismic region including fault, tunnel, and associated local site.

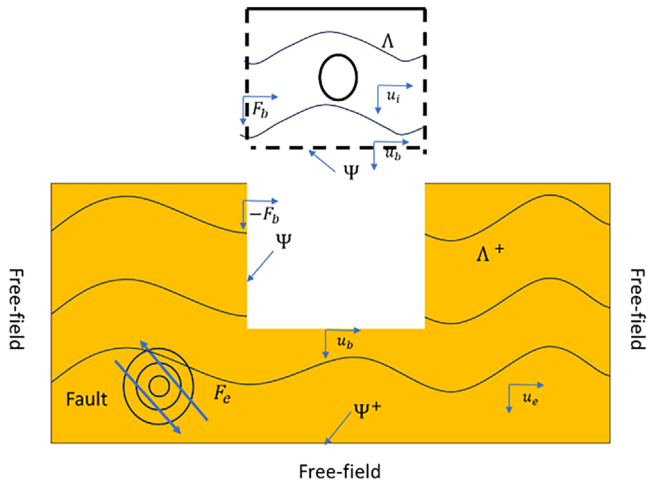


FIGURE 3 The region is partitioned into two subdomains.

efficiency in advanced simulation problems. Corigliance et al.[35] investigated the deep-tunnel response in a near-fault earthquake scenario. Kontoe et al.[36] discussed the seismic response of a soil retaining system comprising a lock camber and three waver-saving basins in the domain. Poursartip et al.[37] proposed a computational tool that integrates the perfectly matched layer and the unstructured spectral elements coupled with the DRM method for analyzing the seismic wave amplification by geological features.

Researchers have made enormous progress in earthquake modeling in recent years.[38–43] However, accurate modeling of soil-fault-structure systems poses several difficulties, such as generating seismic ground motion in the numerical model, different spatial and temporal scales, complex geological features (i.e., topographic irregularities, structures), and soil nonlinearity in the domain. The following challenges are foreseen in modeling the tunnel-fault-soil system:

- Numerical modeling of fault rupture mechanism (i.e., seismic energy release, dip angle, fault length, slip rate) in the domain with appropriate scale.
- The wave in the near-fault earthquake simulation is complex due to body waves of different incident angles and surface waves (if incident angle > critical incident angle).
- Implementing a non-reflecting boundary at the truncated interface for absorbing scattered waves.
- Proper modeling of DRM with accurate computation of DRM layer nodal forces.

The paper is formatted in the following manner. The following section illustrates the DRM formulation and numerical validation for free-field and near-field scenarios. In Section 3, we discuss the Monte Carlo approach for generating stochastic parameters. Section 4 discusses stochastic analysis results for three different soils based on NEHRP provision (i.e., soft, medium, and hard soil). Most importantly, we explain the structural response and its cause to prevent this failure. In the end, a summary and conclusion is provided.

2 | FORMULATION OF MODIFIED DOMAIN REDUCTION METHOD

We follow domain reduction methodology as proposed by Bielak et al.[30] and Yoshimura et al.[31] A semi-infinite region with geological features, earthquake source, propagation path, and the tunnel is illustrated in Figure 1. Since the source-site distance is far away from the localized region of interest, a virtual boundary Ψ is used to divide the semi-infinite region into two parts: Λ and Λ^+. Λ contains the localized feature of interest, like structure and topography. Λ^+ contains the infinite medium, including a seismic source (i.e., fault). The nodal displacement field for the exterior domain Λ^+, boundary Ψ and the interior domain Λ is depicted in Figure 2 by u_i (internal), u_b (common boundary) and u_e (external), respectively. The displacement of u_b on the DRM layer Ψ is continuous and F_b are the nodal forces transferred from Λ^+ to Λ (Figure 3). The equation of motion for the whole semi-infinite domain system given is as follows:

$$M\ddot{u} + C\dot{u} + Ku = F_{ext} \tag{1}$$

where M, C, K and F_{ext} denote mass, damping, stiffness, and external force terms respectively.

Domains Λ and Λ^+ are discretized using finite element method as follows:

$$\begin{bmatrix} M_{ii}^{\Lambda} & M_{ib}^{\Lambda} \\ M_{bi}^{\Lambda} & M_{bb}^{\Lambda} \end{bmatrix} \begin{bmatrix} \ddot{u}_i \\ \ddot{u}_b \end{bmatrix} + \begin{bmatrix} C_{ii}^{\Lambda} & C_{ib}^{\Lambda} \\ C_{bi}^{\Lambda} & C_{bb}^{\Lambda} \end{bmatrix} \begin{bmatrix} \dot{u}_i \\ \dot{u}_b \end{bmatrix} + \begin{bmatrix} K_{ii}^{\Lambda} & K_{ib}^{\Lambda} \\ K_{bi}^{\Lambda} & K_{bb}^{\Lambda} \end{bmatrix} \begin{bmatrix} u_i \\ u_b \end{bmatrix} = \begin{bmatrix} 0 \\ F_b \end{bmatrix} \text{ in } \Lambda \tag{2}$$

$$\begin{bmatrix} M_{bb}^{\Lambda^+} & M_{be}^{\Lambda^+} \\ M_{eb}^{\Lambda^+} & M_{ee}^{\Lambda^+} \end{bmatrix} \begin{bmatrix} \ddot{u}_b \\ \ddot{u}_e \end{bmatrix} + \begin{bmatrix} C_{bb}^{\Lambda^+} & C_{be}^{\Lambda^+} \\ C_{eb}^{\Lambda^+} & C_{ee}^{\Lambda^+} \end{bmatrix} \begin{bmatrix} \dot{u}_b \\ \dot{u}_e \end{bmatrix} + \begin{bmatrix} K_{bb}^{\Lambda^+} & K_{be}^{\Lambda^+} \\ K_{eb}^{\Lambda^+} & K_{ee}^{\Lambda^+} \end{bmatrix} \begin{bmatrix} u_b \\ u_e \end{bmatrix} = \begin{bmatrix} -F_b \\ F_e \end{bmatrix} \text{ in } \Lambda^+ \tag{3}$$

where i, b, and e indices represent the interior, boundary, and exterior nodes; superscripts Λ and Λ^+ define the region to which the block matrix corresponds to. The global matrix equation for the entire domain is obtained by combining Equations (2) and (3):

$$\begin{bmatrix} M_{ii}^{\Lambda} & M_{ib}^{\Lambda} & 0 \\ M_{bi}^{\Lambda} & M_{bb}^{\Lambda} + M_{bb}^{\Lambda^+} & M_{be}^{\Lambda^+} \\ 0 & M_{eb}^{\Lambda^+} & M_{ee}^{\Lambda^+} \end{bmatrix} \begin{bmatrix} \ddot{u}_i \\ \ddot{u}_b \\ \ddot{u}_e \end{bmatrix} + \begin{bmatrix} C_{ii}^{\Lambda} & C_{ib}^{\Lambda} & 0 \\ C_{bi}^{\Lambda} & C_{bb}^{\Lambda} + C_{bb}^{\Lambda^+} & C_{be}^{\Lambda^+} \\ 0 & C_{eb}^{\Lambda^+} & C_{ee}^{\Lambda^+} \end{bmatrix} \begin{bmatrix} \dot{u}_i \\ \dot{u}_b \\ \dot{u}_e \end{bmatrix} + \begin{bmatrix} K_{ii}^{\Lambda} & K_{ib}^{\Lambda} & 0 \\ K_{bi}^{\Lambda} & K_{bb}^{\Lambda} + K_{bb}^{\Lambda^+} & K_{be}^{\Lambda^+} \\ 0 & K_{eb}^{\Lambda^+} & K_{ee}^{\Lambda^+} \end{bmatrix} \begin{bmatrix} u_i \\ u_b \\ u_e \end{bmatrix} = \begin{bmatrix} 0 \\ 0 \\ F_e \end{bmatrix} \tag{4}$$

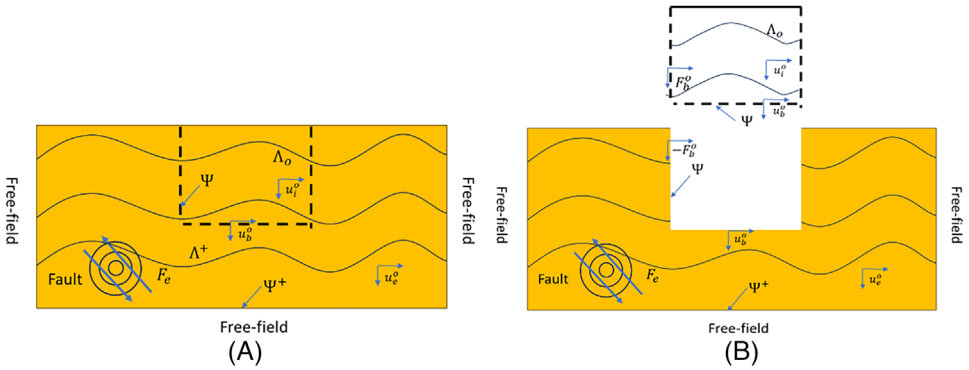


FIGURE 4 Auxiliary problem: (A) localized region of interest is removed by auxiliary region and (B) auxiliary seismic region partitioned into two subdomains.

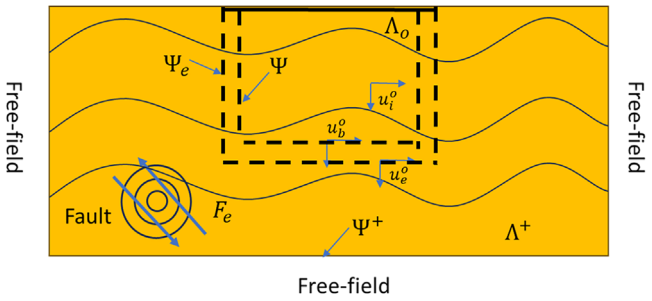


FIGURE 5 DRM method for a tunnel-soil system. The first step: the model defines the auxiliary problem over the localized region of the model domain.

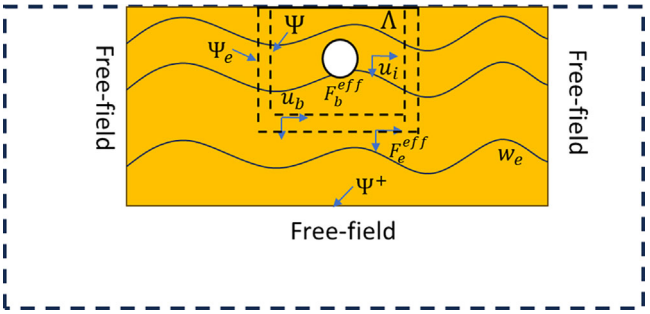


FIGURE 6 DRM method for a tunnel-soil system. The second step: The model is defined over the reduced region.

To transfer the seismic ground motion from the fault to the boundary Ψ, an auxiliary problem (in Figure 4) is considered to replace the localized region of interest with an auxiliary region. The internal domain is denoted as Λ^o, where the structure is removed. The nodal displacements and boundary forces are denoted as u_b^o, u_i^o, u_e^o and F_b^o. The equation of motion for Λ^+ in the auxiliary problem is as follows:

$$\begin{bmatrix} M_{bb}^{\Lambda^+} & M_{be}^{\Lambda^+} \\ M_{eb}^{\Lambda^+} & M_{ee}^{\Lambda^+} \end{bmatrix} \begin{bmatrix} \ddot{u}_b^o \\ \ddot{u}_e^o \end{bmatrix} + \begin{bmatrix} C_{bb}^{\Lambda^+} & C_{be}^{\Lambda^+} \\ C_{eb}^{\Lambda^+} & C_{ee}^{\Lambda^+} \end{bmatrix} \begin{bmatrix} \dot{u}_b^o \\ \dot{u}_e^o \end{bmatrix} + \begin{bmatrix} K_{bb}^{\Lambda^+} & K_{be}^{\Lambda^+} \\ K_{eb}^{\Lambda^+} & K_{ee}^{\Lambda^+} \end{bmatrix} \begin{bmatrix} u_b^o \\ u_e^o \end{bmatrix} = \begin{bmatrix} -F_b^o \\ F_e \end{bmatrix} \text{ in } \Lambda^+ \tag{5}$$

The second equation in Equation (5) can be written in terms of free-field variables at the boundary Ψ:

$$F_e = M_{eb}^{\Lambda+}\ddot{u}_b^o + M_{ee}^{\Lambda+}\ddot{u}_e^o + C_{eb}^{\Lambda+}\dot{u}_e^o + K_{eb}^{\Lambda+}u_b^o + K_{ee}^{\Lambda+}u_e^o \tag{6}$$

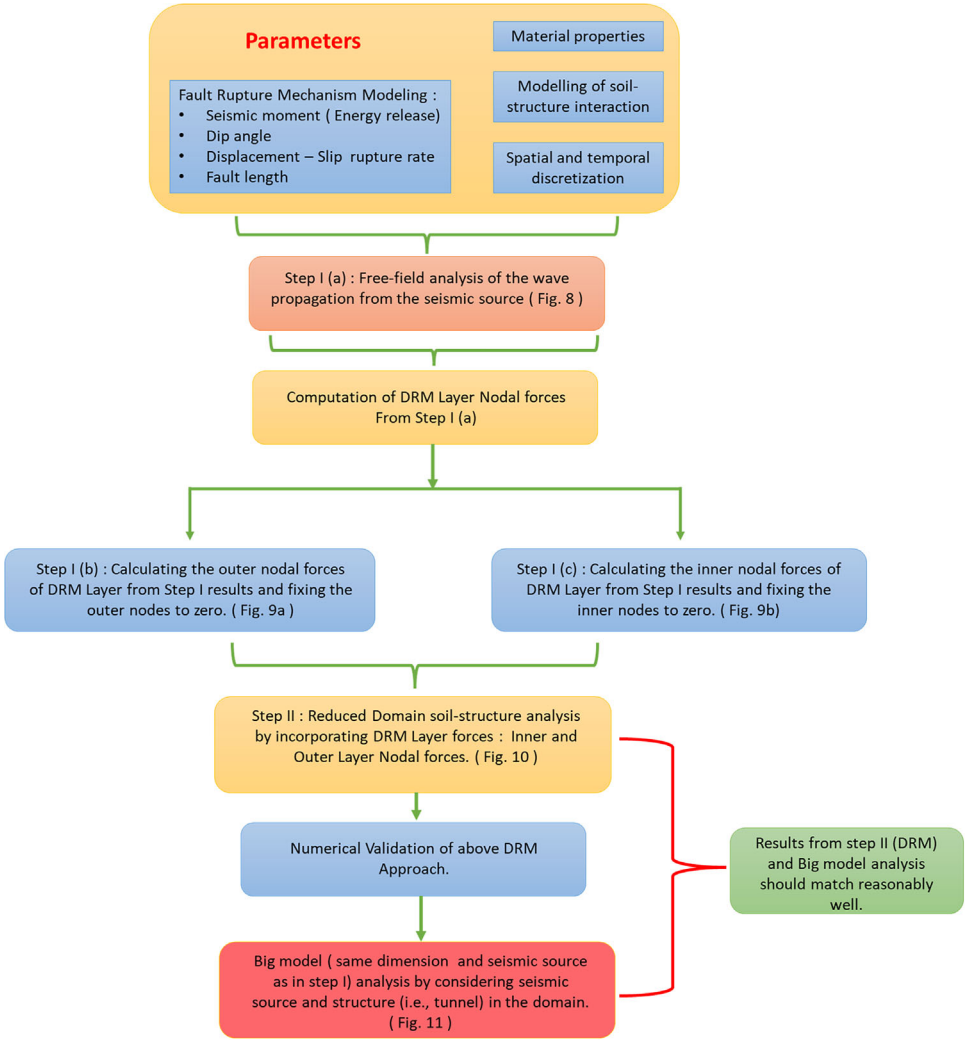


FIGURE 7 The schematic flow-chart of implementing DRM algorithm in MASTODON.

The total displacement u_e can be rewritten as the sum of the free-field u_e^o and the residual term w_e as follows:

$$u_e = u_e^o + w_e \tag{7}$$

By substituting Equations (7) into (2) and transferring the free-field terms to the right-side results in:

$$\begin{bmatrix} M_{ii}^{\Lambda} & M_{ib}^{\Lambda} & 0 \\ M_{bi}^{\Lambda} & M_{bb}^{\Lambda} + M_{bb}^{\Lambda^+} & M_{be}^{\Lambda^+} \\ 0 & M_{eb}^{\Lambda^+} & M_{ee}^{\Lambda^+} \end{bmatrix} \begin{bmatrix} \ddot{u}_i \\ \ddot{u}_b \\ \ddot{w}_e \end{bmatrix} + \begin{bmatrix} C_{ii}^{\Lambda} & C_{ib}^{\Lambda} & 0 \\ C_{bi}^{\Lambda} & C_{bb}^{\Lambda} + C_{bb}^{\Lambda^+} & C_{be}^{\Lambda^+} \\ 0 & C_{eb}^{\Lambda^+} & C_{ee}^{\Lambda^+} \end{bmatrix} \begin{bmatrix} \dot{u}_i \\ \dot{u}_b \\ \dot{w}_e \end{bmatrix} +$$
$$\begin{bmatrix} K_{ii}^{\Lambda} & K_{ib}^{\Lambda} & 0 \\ K_{bi}^{\Lambda} & K_{bb}^{\Lambda} + K_{bb}^{\Lambda^+} & K_{be}^{\Lambda^+} \\ 0 & K_{eb}^{\Lambda^+} & K_{ee}^{\Lambda^+} \end{bmatrix} \begin{bmatrix} u_i \\ u_b \\ w_e \end{bmatrix} = \begin{bmatrix} 0 \\ -M_{be}^{\Lambda^+} \ddot{u}_e^0 - C_{be}^{\Lambda^+} \dot{u}_e^0 - K_{be}^{\Lambda^+} u_e^0 \\ -M_{ee}^{\Lambda^+} \ddot{u}_e^0 - C_{ee}^{\Lambda^+} \dot{u}_e^0 - K_{ee}^{\Lambda^+} u_e^0 + F_e \end{bmatrix} \tag{8}$$

By substituting Equations (6) into (8), the final equation is:

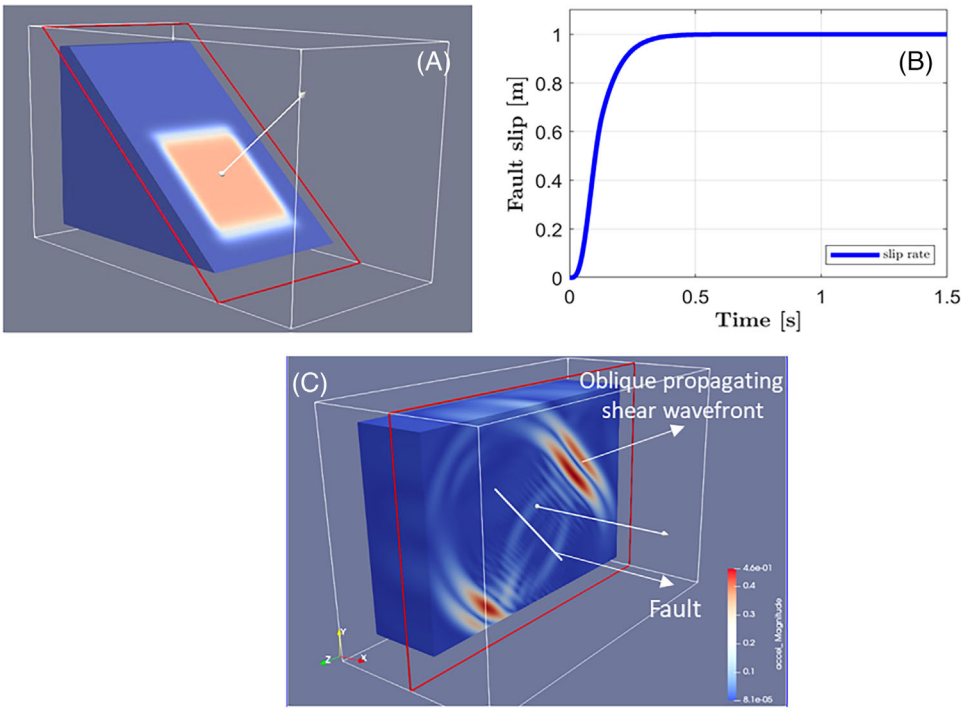


FIGURE 8 (A) Sectional view of the planar seismic fault showing the point sources,[42] (B) Slip-displacement time history for the seismic fault,[42] and (C) Free-field analysis of fault rupture (inclined at 45°) showing oblique propagating shear wavefront.

TABLE 1 Seismic source parameters.

Inclination angle (dip)	45°
Rake	90°
Shear modulus (GPa)	1.996e7
Point sources	16032
Slip rate	Uniform
Fault dimension (L × W)	425 m × 300 m

TABLE 2 Material parameters.

Shear wave velocity (m/s)	1000
Density (kg/m^3)	1700
Poisson's ratio	0.3
Damping ratio (%)	3

$$\begin{bmatrix} 0 & M_{ib}^{\Lambda} & 0 \\ M_{ii}^{\Lambda} & M_{bb}^{\Lambda} + M_{bb}^{\Lambda^+} & M_{be}^{\Lambda^+} \\ M_{bi}^{\Lambda} & M_{eb}^{\Lambda^+} & M_{ee}^{\Lambda^+} \end{bmatrix} \begin{bmatrix} \ddot{u}_i \\ \ddot{u}_b \\ \ddot{w}_e \end{bmatrix} + \begin{bmatrix} C_{ii}^{\Lambda} & C_{ib}^{\Lambda} & 0 \\ C_{bi}^{\Lambda} & C_{bb}^{\Lambda} + C_{bb}^{\Lambda^+} & C_{be}^{\Lambda^+} \\ 0 & C_{eb}^{\Lambda^+} & C_{ee}^{\Lambda^+} \end{bmatrix} \begin{bmatrix} \dot{u}_i \\ \dot{u}_b \\ \dot{w}_e \end{bmatrix} + \begin{bmatrix} K_{ii}^{\Lambda} & K_{ib}^{\Lambda} & \\ K_{bi}^{\Lambda} & K_{bb}^{\Lambda} + K_{bb}^{\Lambda^+} & K_{be}^{\Lambda^+} \\ 0 & K_{eb}^{\Lambda^+} & K_{ee}^{\Lambda^+} \end{bmatrix} \begin{bmatrix} u_i \\ u_b \\ w_e \end{bmatrix} = \begin{bmatrix} 0 \\ -M_{be}^{\Lambda^+} \ddot{u}_e^0 - C_{be}^{\Lambda^+} \dot{u}_e^0 - K_{be}^{\Lambda^+} u_e^0 \\ -M_{eb}^{\Lambda^+} \ddot{u}_b^0 - C_{eb}^{\Lambda^+} \dot{u}_b^0 - K_{eb}^{\Lambda^+} u_b^0 \end{bmatrix} \tag{9}$$

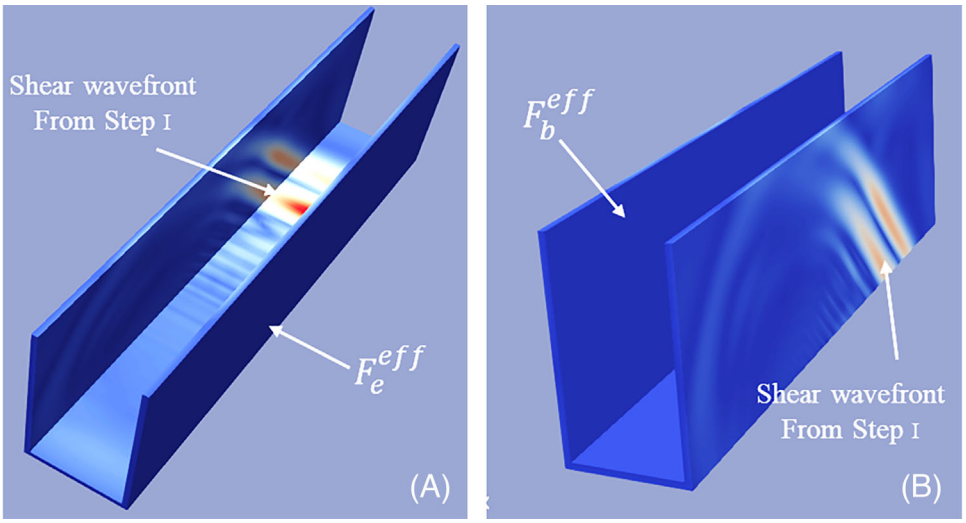


FIGURE 9 DRM layer forces (A) outer layer and (B) inner layer.

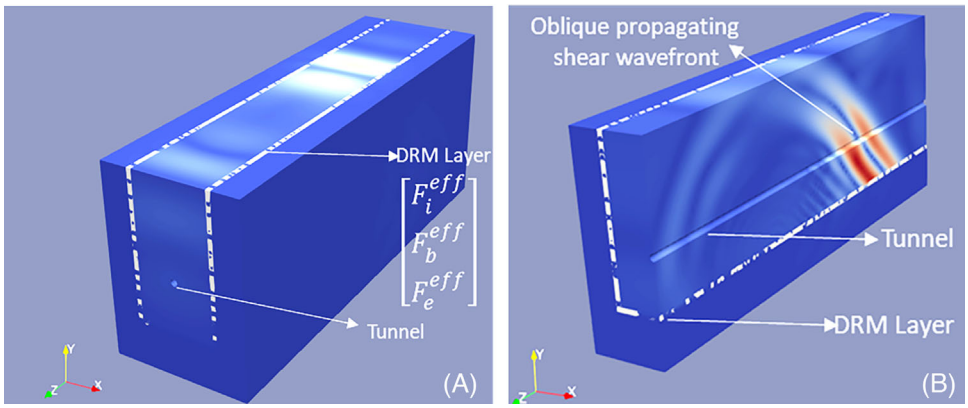


FIGURE 10 Small model with DRM (A) 3D view and (B) longitudinal sectional view.

The mass-matrix, damping-matrix, and stiffness-matrix on the left-hand side of Equation (9) are the same as that in Equation (4). Therefore, the seismic force F_e is replaced by effective nodal forces F^{eff} as given below:

$$F^{eff} = \begin{bmatrix} F_i^{eff} \\ F_b^{eff} \\ F_e^{eff} \end{bmatrix} = \begin{bmatrix} 0 \\ -M_{be}^{\Lambda^+}\ddot{u}_e^o - C_{be}^{\Lambda^+}\dot{u}_e^o - K_{be}^{\Lambda^+}u_e^0 \\ M_{eb}^{\Lambda^+}\ddot{u}_b^o + C_{eb}^{\Lambda^+}\dot{u}_e^o + K_{eb}^{\Lambda^+}u_b^0 \end{bmatrix} \tag{10}$$

The sub-matrixes $M_{be}, K_{be}, C_{be}, M_{eb}, C_{eb}$, and K_{eb} vanishes at all points in the domain Λ^+, except for the boundary nodes which belongs to Ψ region. Hence, the effective force of the DRM layer in the auxiliary problem is given in Equation (10).

2.1 | Verification of modified DRM with numerical problem

The semi-infinite seismic region comprises of seismic fault, localized geological features (such as tunnels, dams, ridges, nuclear power plants and other important structures) and their associated local sites (Figure 2). The wide spatial separation between the localized geological feature (tunnel) and the seismic source of excitation makes the computational domain size large. Consequently, full-scale numerical simulation tends to be computationally expensive and inefficient. And this

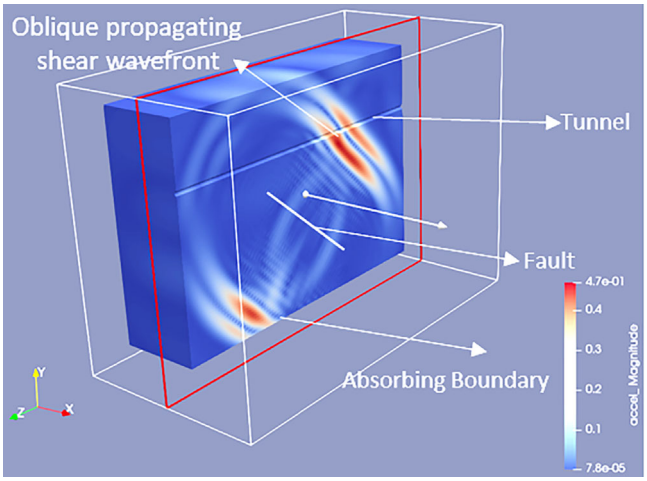


FIGURE 11 The big model with the tunnel-soil-fault system.

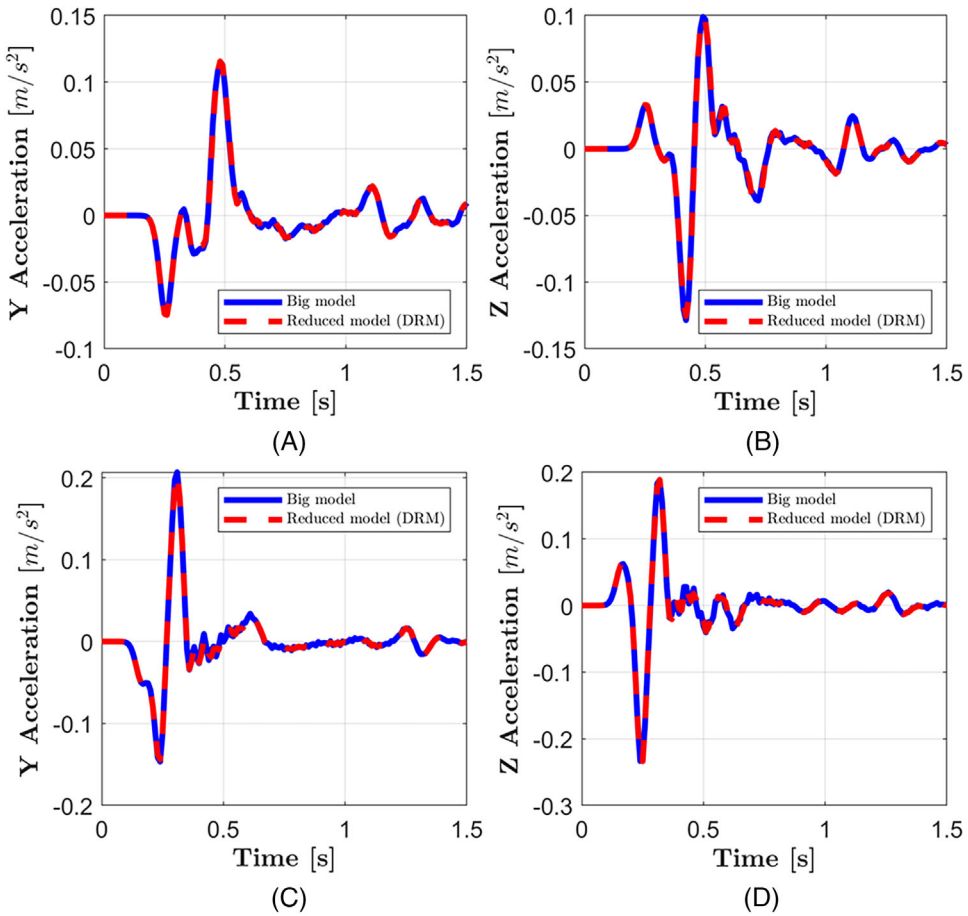


FIGURE 12 Acceleration comparison at (A, B) X = 500 m, Y = 700 m, and Z = 500 m; (C, D) X = 500 m, Y = 550 m, and Z = 500 m: (A, C) Y-component and (B, D) Z-component of acceleration, respectively.

necessitates an alternative approach which tends to approximate the structural dynamics by systematically breaking down the problem of solving the large single model into two sequential steps which is the basis of DRM.

In Step I of DRM, we consider a background structure with seismic fault (domains Λ_o and Λ^+), and deleting the localized geological features (refer to Figure 5). Then, a free-field analysis is carried out on this background structure to compute the seismic ground motion (u^o, $\dot{u}^o$, $\ddot{u}^o$). This computation has to be performed only one time for a particular seismic

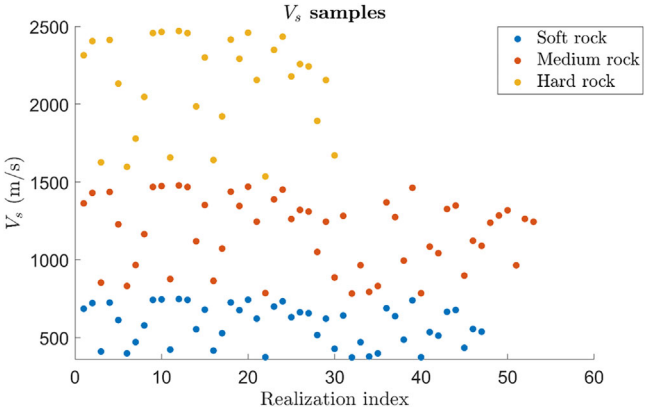


FIGURE 13 Shear velocity (Vs) realizations.

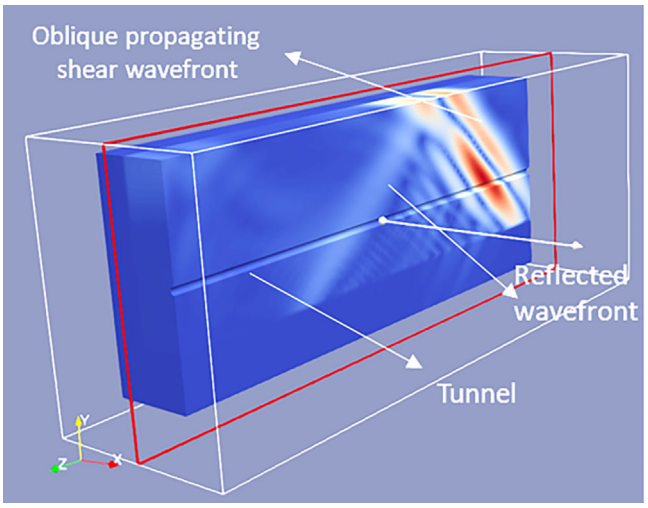


FIGURE 14 Small model having complex wave field in the domain.

source configuration. The seismic ground motion computed in step I is then used to determine the localized equivalent nodal forces (F^{eff}) on the DRM layer, that is, the region enclosed by layers Ψ and Ψ_e borders (refer to Figure 5).

In Step II of DRM, we consider only the reduced DRM model containing the localized region of interest with structure, defined by $\Lambda \cup \hat{\Lambda}^+$ (see Figure 6). The DRM layer forces are applied as input over the reduced DRM model and then near-field analysis is performed to determine the local structural response (i.e., u_i in Λ region, u_b in Ψ region, and residual displacement field w_e in $\hat{\Lambda}^+$). It ought to be noted that only step II (Reduced DRM model) needs to be repeated if any material or geometric parameters within the area of interest have to be varied.

We have extended the pre-existing 2D implementation of DRM in the open source finite element (FE) package MASTODON (Multi-hazard Analysis for STOchastic time DOmaiN phenomena)[44] based on MOOSE framework[45] to 3D. Figure 7 represents the schematic flow-chart of the numerical implementation of the DRM in the finite element software.

A 3D half-space domain with a seismic source (i.e., fault rupture) is considered for free-field numerical analysis (in Figure 8C). The model of dimensions 500 m × 700 m × 1000 m is considered for step I(a), according to Figure 7. To model fault rupture in MASTODON, the fault is discretized into a finite number of point sources (Figure 8A), and the moment matrix $M_o(p,t)$ is calculated for each point source (p) and each time instant (t) using the *Seismic Source Object*.[44] The seismic moment $M_o(p,t)$ of the earthquake fault rupture is as follows

$$M_0(p,t) = \mu A \bar{u}(p,t) \tag{11}$$

where μ = shear modulus of soil, A = area of fault rupture, and $\bar{u}(p,t)$ = averaged slip-displacement rate of the fault (Figure 8B). The modeling parameters for seismic fault are listed in Table 1.

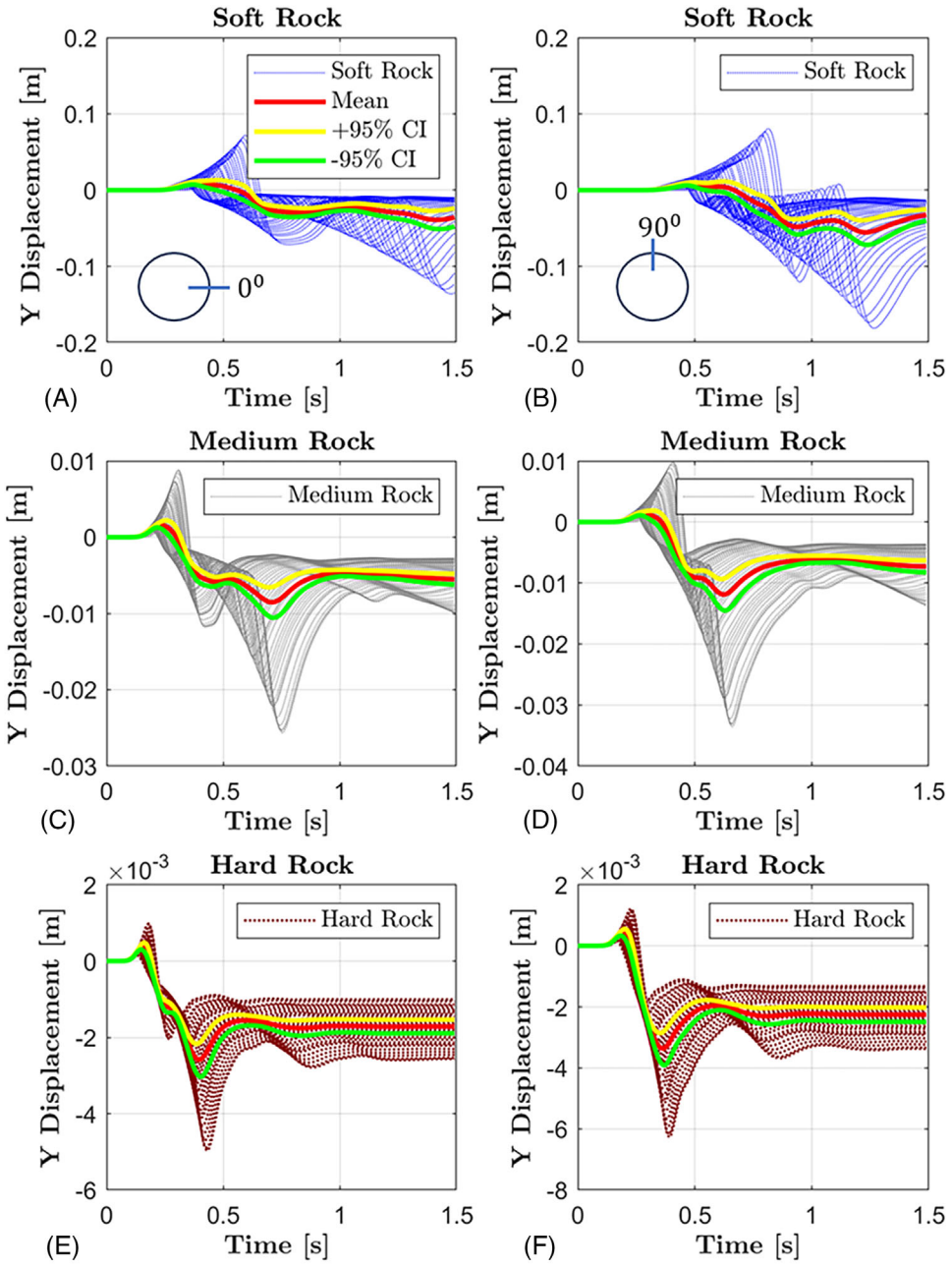


FIGURE 15 Y displacement time histories of output ground motion for different rock media at different locations 0° (A,C,E) and at 90° (B,D,F). Mean value of displacement is given by curve in red, +95% and −95 % confidence interval curves are labeled in yellow and green respectively.

The rock medium is assumed to be homogenous and linear elastic, and the material properties are tabulated in Table 2. The Newmark-β method[46] is used for implicit time integration with integration parameters as $\beta = 0.25$ and $\gamma = 0.5$ for which the method is unconditionally stable. We used 8-node brick elements to mesh the computational domain and 6-node prism elements in the vicinity of the tunnel structure. This study considers ten nodes per wavelength scheme[16] for determining the optimal mesh size. The viscous absorbing boundary[17] is prescribed on all the boundaries (except the top surface) to dissipate the residual waves in the domain. The simulation was done for 1.5 s. The computational time for the big model simulation was 4.5 h while the DRM model took around 1.5 h.

For steps I(b) and step I(c) (according to Figure 7), a single-layer DRM (Figure 9) is modeled for obtaining the effective nodal forces (Equation 10) from step I(a). To obtain F_e^{eff}, we need to prescribe zero displacement to outer nodes and

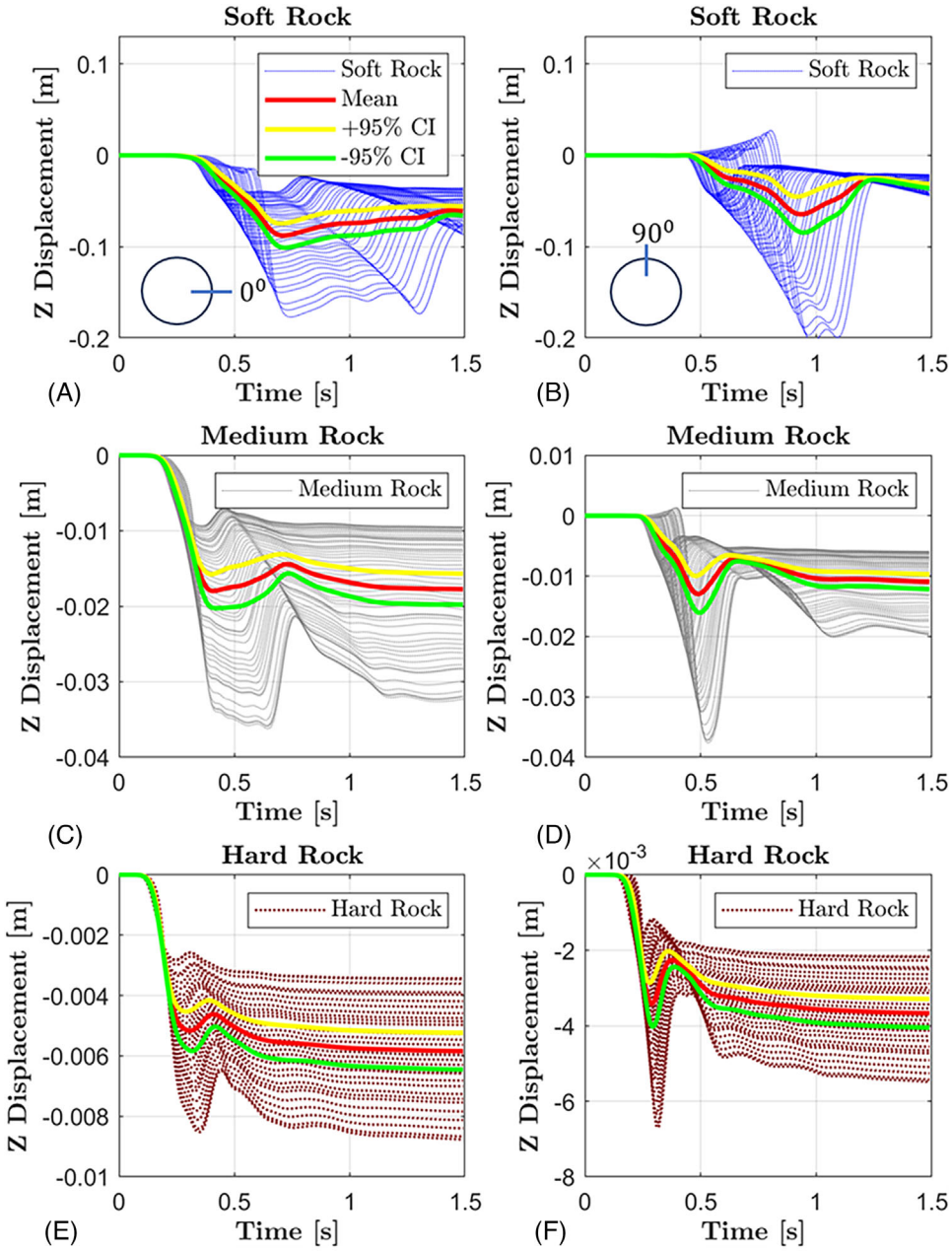


FIGURE 16 Z displacement time histories of output ground motion for different rock media at different locations 0° (A,C,E) and at 90° (B,D,F).

calculate outer node boundary forces from step I(a) (Figure 9A). Similarly, for calculating F_b^{eff}, we need to prescribe zero displacements to inner nodes and calculate inner node boundary forces from step I(a) (Figure 9B).

A reduced 3D model dimension of 160 m × 300 m × 1000 m is considered with a unlined tunnel diameter of 15 m for analysis of step II (Figure 10). The DRM layer effective nodal forces. F^{eff} calculated in steps I(b) and step I(c) is used as a seismic source for step II (reduced domain) simulation.

To verify the above analysis, we ran a verification simulation on a big model with dimensions 500 m × 700 m × 1000 m (Figure 11) with fault and tunnel in the domain. The results obtained in steps II and big model match reasonably well throughout the domain.

Acceleration time histories at [X = 500 m, Y = 700 m, and Z = 500 m] and [X = 500 m, Y = 550 m, and Z = 500 m] point are shown in Figure 12. It can be observed that the results obtained in big model with the fault-tunnel system perfectly match those obtained in step II (reduced domain (near-field) with DRM layer effective nodal forces).

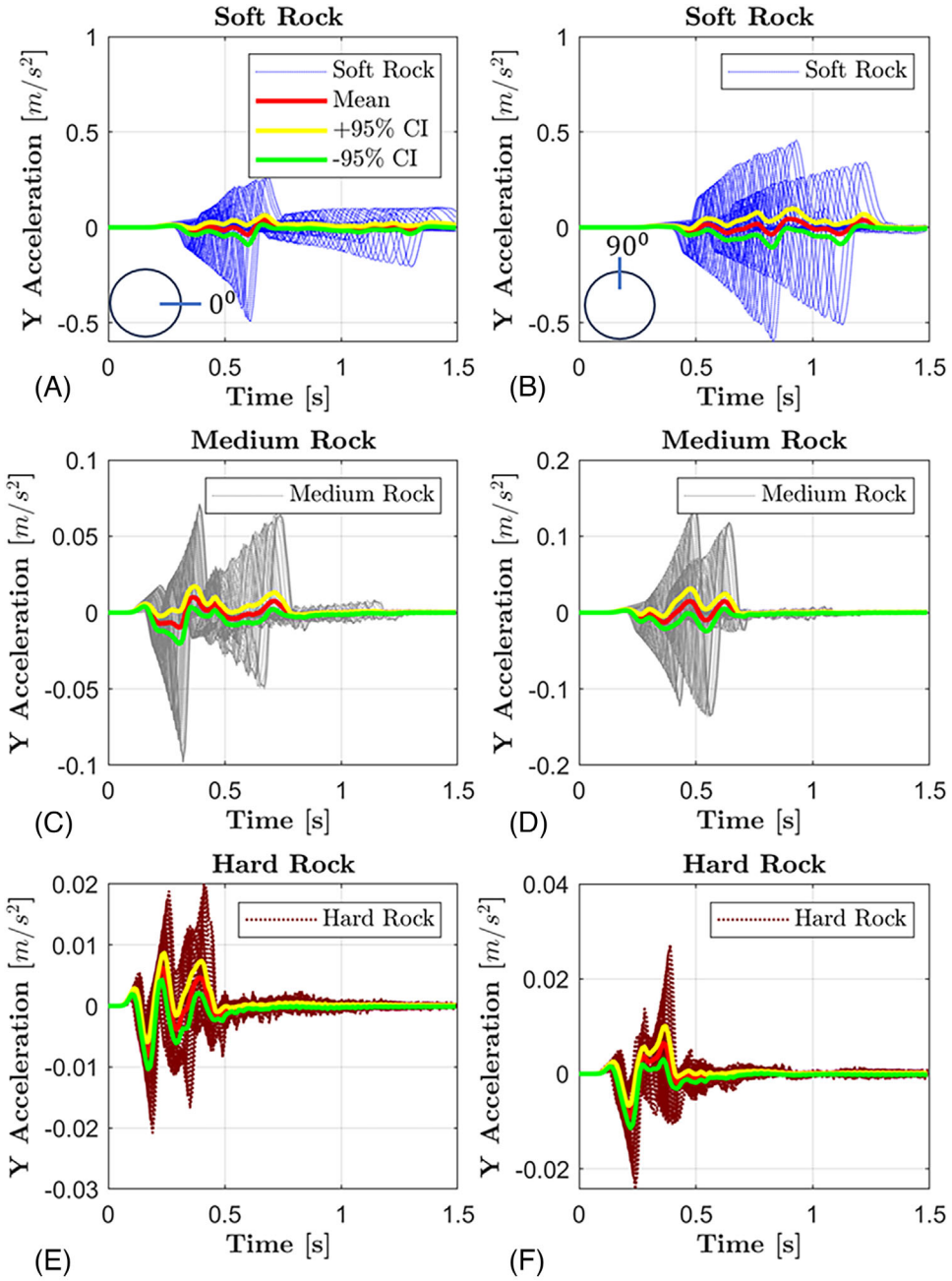


FIGURE 17 Y acceleration time histories of output ground motion for different rock media at different locations 0° (A,C,E) and at 90° (B,D,F).

The above observation and results verify the efficacy of the DRM. Henceforth, we shall be employing DRM for all the simulations.

3 | STOCHASTIC MODELING

The shear velocities V_s were sampled from a uniform probability distribution corresponding to three different rock samples, $V_s \sim U(V_{s,min}, V_{s,max})$ where $V_{s,min}$ and $V_{s,max}$ are the minimum and maximum shear wave velocities corresponding to a particular rock medium, based on NEHRP datasheet. We considered 130 realizations of V_s for three rock domains, which in the order of increasing stiffness are, soft (i.e., 47 samples), medium (i.e., 53 samples) and hard (i.e., 30 samples) as shown in Figure 13. We performed quasi-Monte Carlo simulations using MASTODON.

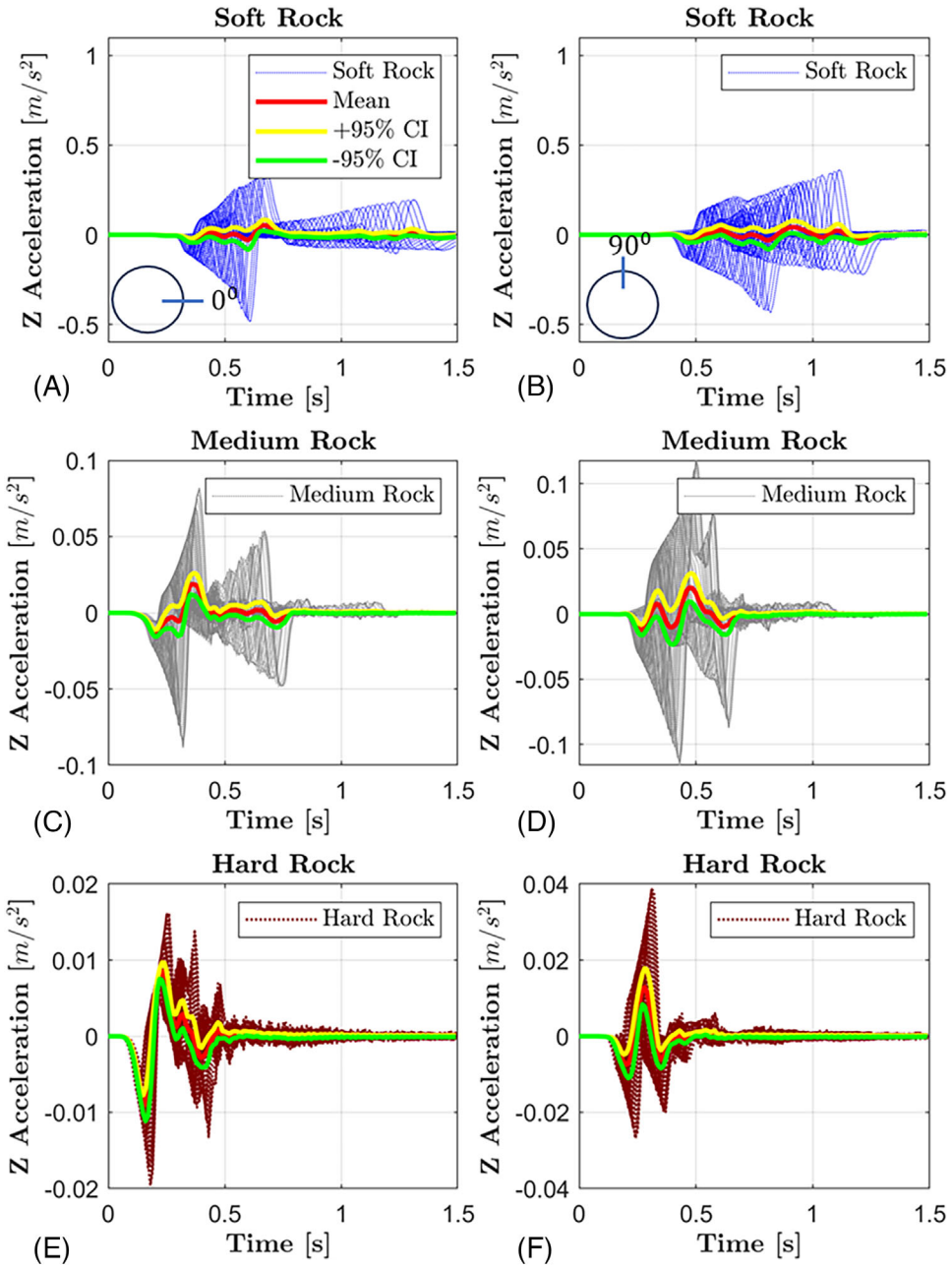


FIGURE 18 Z acceleration time histories of output ground motion for different rock media at different locations 0° (A,C,E) and at 90° (B,D,F).

4 | RESULTS AND DISCUSSION

We performed the simulation of every realization for a time duration of 1.5 s such that seismic wave propagation, its interaction with tunnel reflection from free surface, and its damping was captured (see Figure 14).

4.1 | Time history

We choose two locations, both lying in the region traversed by the seismic wave, to record the time evolution. They are located 0° and 90° degrees with respect to X-axis on the periphery of the tunnel at a longitudinal distance Z = 600 m.

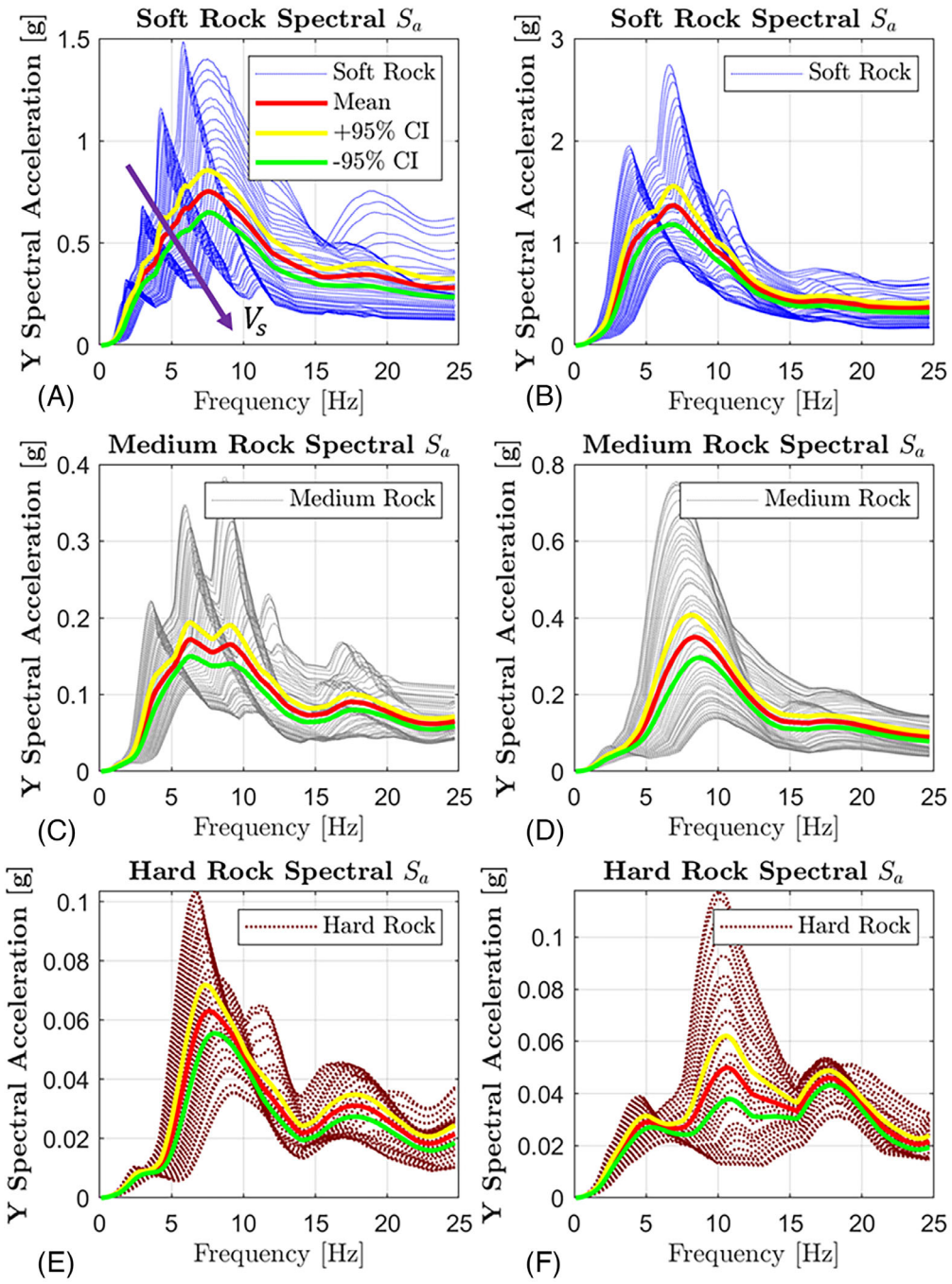


FIGURE 19 Y spectral acceleration of output ground motion for different rock media at different locations 0° (A,C,E) and at 90° (B,D,F).

4.1.1 | Displacement time history

The tunnel undergoes motion in the Y-Z plane which proceeds via three stages. Initially, the amplitude of both Y- and Z-components of displacement is low. Then, it gradually builds up till it reaches a peak and eventually the motion starts to decay due to dissipation of seismic energy as a result of material damping. The decay process is also assisted by the absorption boundary conditions. From Figures 15–16, it is inferred that the peak value of the Y-component of the displacement is not in phase with that of the Z-component and the former follows the latter.

The displacement value decreases by an order of magnitude as the shear modulus of the medium increases, that is, from soft to medium to hard rock. We also observe that the peak displacement is attained first in hard rock, then in medium rock and last in soft rock. Furthermore, Figures 15 and 16 shows that increase in V_s tends to negatively impact

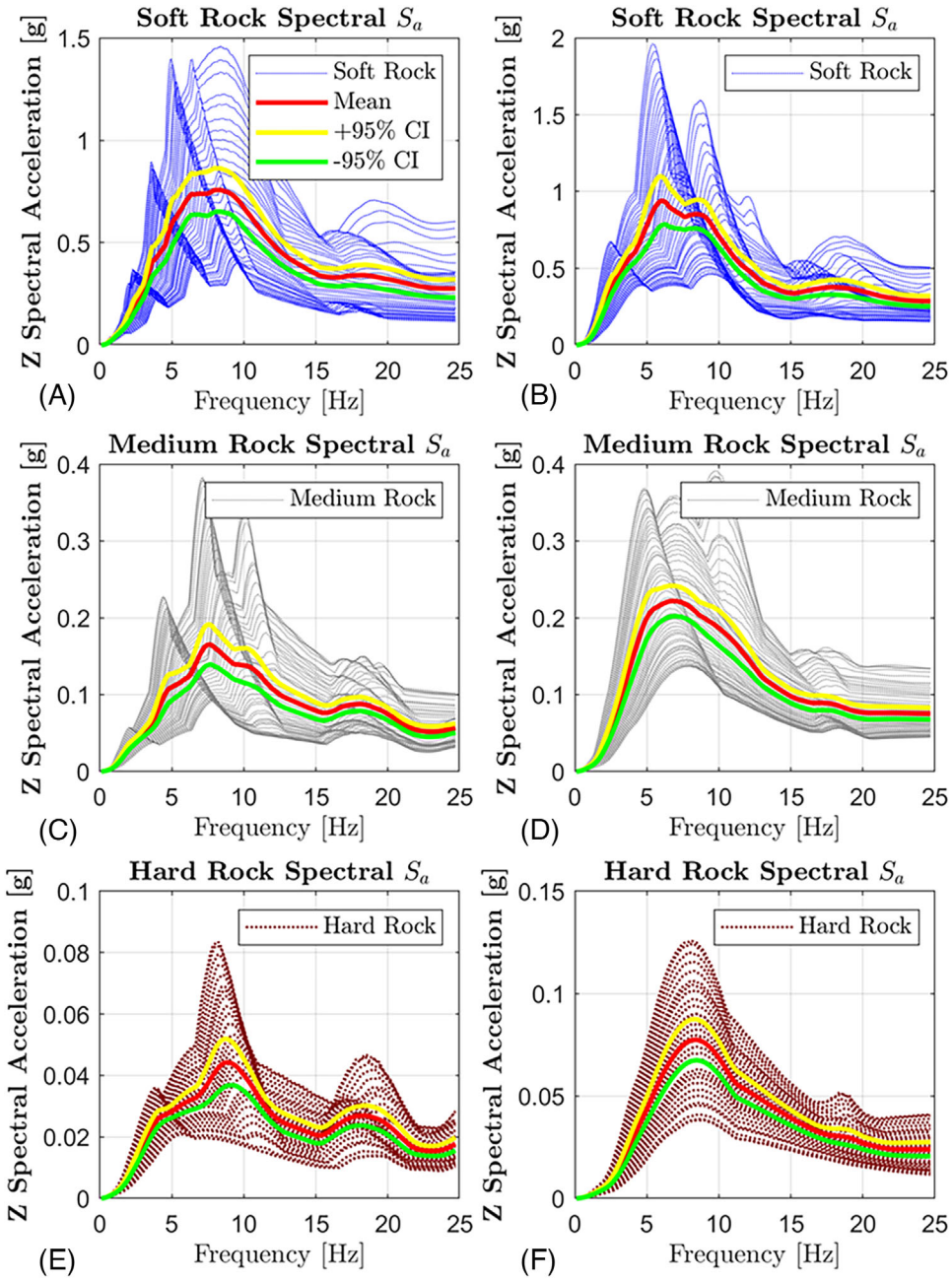


FIGURE 20 Z spectral acceleration of output ground motion for different rock media at different locations 0° (A,C,E) and at 90° (B,D,F).

the displacement behavior and hastens the occurrence of peak amplitude for all the media. The motion tends to subside sooner as V_s increases. This could be attributed to inertia of the medium which determines its reaction time.

4.1.2 | Acceleration time history

It can be inferred from Figures 17 and 18 that the components of acceleration reaches its maximum earliest in hard rock followed by medium and then soft rocks, similar to the trend observed for displacement time history.

Increasing V_s reduces the magnitude of the acceleration and hastens the formation of peak value (see Figures 17 and 18). However, an interesting observation can be made for acceleration response such that the aperiodic-like variations increases in severity as we move from soft to hard rocks.

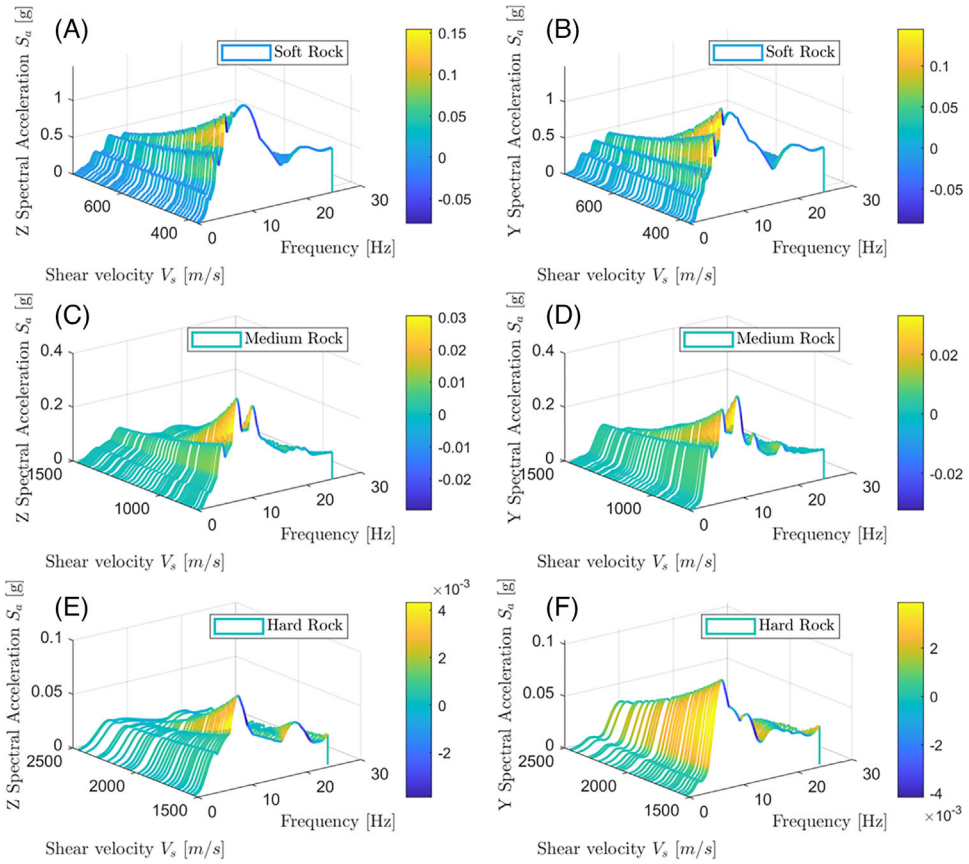


FIGURE 21 Z spectral acceleration response behavior for different rock media at different locations 0° (A,C,E) and at 90° (B,D,F).

4.2 | Spectral analysis

Figures 19 and 20 shows spectral plots of the Y- and Z-components of acceleration for the three media. With increasing V_s, we observe multimodal dynamics at play. For the case of soft rock, the peak broadband frequency tends to decay with an increase in V_s. In contrast, the lower peaks get retained, albeit with frequency shift. Similar patterns exist for both medium and hard rocks. The frequency peaks become lesser in number as the stiffness of the rock medium increases. In higher frequencies, the energy dissipation is high, resulting in no peaks for higher frequencies. Broadband shifts toward the lower frequency side, and peak frequencies eventually merge into that.

Furthermore, we analyze the dynamics of peak frequencies (f_{peak}). The evolution of f_{peak} mimics mode-like behavior. In Figures 19 and 20, there are four predominant peaks at lower V_s for soft rock but we observe a gradual growth of one much more powerful peak at higher V_s. The maximum intensity decreases with increasing V_s, implying that energy gets redistributed at higher V_s. A linear relationship between f_{peak} and V_s can easily be deduced for the soft rock sample (see Figures 19 and 20). This could be attributed to the tunnel length being comparable to the wavelength of the input ground motion. This observation highlights that highly nonlinear structure-wave interactions could also produce a linear variation. However, this linear trend breaks down with the progression in the shear modulus of rock samples.

For the 90° location (see Figure 21B,D,F), a broadband peak spectrum is seen for all the rock samples which gradually spreads with increase in V_s. This could be due to complex wave interactions with the reflection of the SV wavefront from the top free boundary.

We observe that the mean of the spectral acceleration response (see red curves in Figures 19 and 20) has peak frequency broadband in all the rock samples. The +95% and −95% confidence interval curves, represented by yellow and green curves respectively, have the similar variation as the mean curve.

4.3 | Spatial variation along the length of the tunnel structure

The wavefronts are very complex due to the presence of body waves of different incident angles and surface waves (if incident angle is more than the critical angle). Based on the nature of variation of spectral acceleration along the longitudinal axis of the tunnel (Figures 22 and 23), we define three primary regions: (a) region dominated by incident waves, (b) region influenced by scattering of waves from the structure, and (c) region influenced by the reflected waves from the free surface. Region (a) ranges from 100 to 400 m. The number of distinct frequency peaks decrease with Z, signifying the gradual concentration of energy in the first peak frequency. In region (b) (450 m – 650 m), although the count of peak frequencies increases slightly due to the emergence of new peaks, we see a decline in the corresponding intensities of spectral acceleration. A proper reason could be due to destructive interference between the incident and reflected-scattered waves. Further, in region (c) which goes from 700 to 1000 m, it is observed that newly emerged peaks have gained prominence and have higher values of spectral acceleration.

It could be attributed to the redistribution of the seismic energy possessed by the reflected SV wavefronts from the free surface among the distinct peaks. We deduce from Figures 22–23 that the spectral acceleration reduces from soft to medium to hard rock domain. This is because the temporal retention of wavefronts in the hard rock is lower than that of soft and medium ones. With increase in V_s, we observe a gradual shift in frequency peaks.

4.4 | Local site effects and deformation modes

Figures 24 and 25 demonstrates the Y spectral displacement profiles for different soil properties along the axis of the tunnel for 0° and 90° locations respectively. Similarly, Figures 26 and 27 represents Z spectral displacement for 0° and 90° locations respectively. Frequency shift for the peak response is observed for different soil profiles. The softer rock domain amplify at lower frequencies, whereas the stiffer domain amplify at higher frequencies. This may be due to the fact that amplification is strongly dependent on the frequency content in the input ground motion. However, very high frequencies are de-amplified (Figure 24). These response spectra plots would be beneficial in determining the peak response of tunnels to earthquakes and their natural frequency can be assessed. Accordingly, we can design the tunnel and damp out the frequencies which resonates with the structure. Due to the complex wavefield in the domain, spectral displacement profiles at 0° and 90° emphasize that tunnel is twisted/rotated in the transverse direction, that is, ovaling deformation of tunnel cross-section (shear wave propagating normal to tunnel axis). As we move along the axis of the tunnel, the spectral displacement first gradually increases, then decreases and then rises again toward the end it again indicating longitudinal bending deformation (seismic wave generates particle motion perpendicular to longitudinal axis).

5 | CONCLUSION

In this paper, we conducted a comprehensive investigation of 3D tunnel response in near-fault ground motion to various rock media (namely, soft, medium and hard) using MASTODON, an open source FE code for soil-structure interaction studies. We extended the pre-existing 2D implementation of DRM in the code to 3D and verified it against big model simulations. DRM is a two-step methodology for reducing the size of computational domain in large-scale seismic wave propagation simulations. The technique has been briefly outlined in Section 2. This algorithm provides efficient and reasonably accurate modeling of seismic source, wave propagation paths, and local site effects. We considered linear elastic solid model. Stochastic modeling was done for every soil considering shear wave velocity (Vs) as the uncertain parameter. We carried out quasi-Monte Carlo simulations for each soil wherein realizations of V_s was selected from uniform distribution of corresponding Vs obtained from on National Earthquake Hazards Reduction Program (NEHRP) datasheet.

We have observed the nature of rock medium and V_s significantly influences the tunnel response. Although the displacement and acceleration values are high for the soft rock, the aperiodicity of the corresponding time histories tend to increase from soft to medium to hard rocks. The uncertainties in the rock medium properties dominate the local site effects. The significance of the uncertainty in V_s can be gauged from the fact that the tunnel motion characteristics is very sensitive to V_s. Toward the lower end of V_s distribution, the seismic wave energy is concentrated in a single frequency broadband. However, it gets gradually transferred to lower distinct frequencies at higher V_s due to complex nonlinear wave interactions. Simultaneously, the peaks undergo a near-linear shift with respect to V_s for the soft and medium rocks. We also observed that there is some nonlinear mechanism induced due to the interaction of waves with free surface and

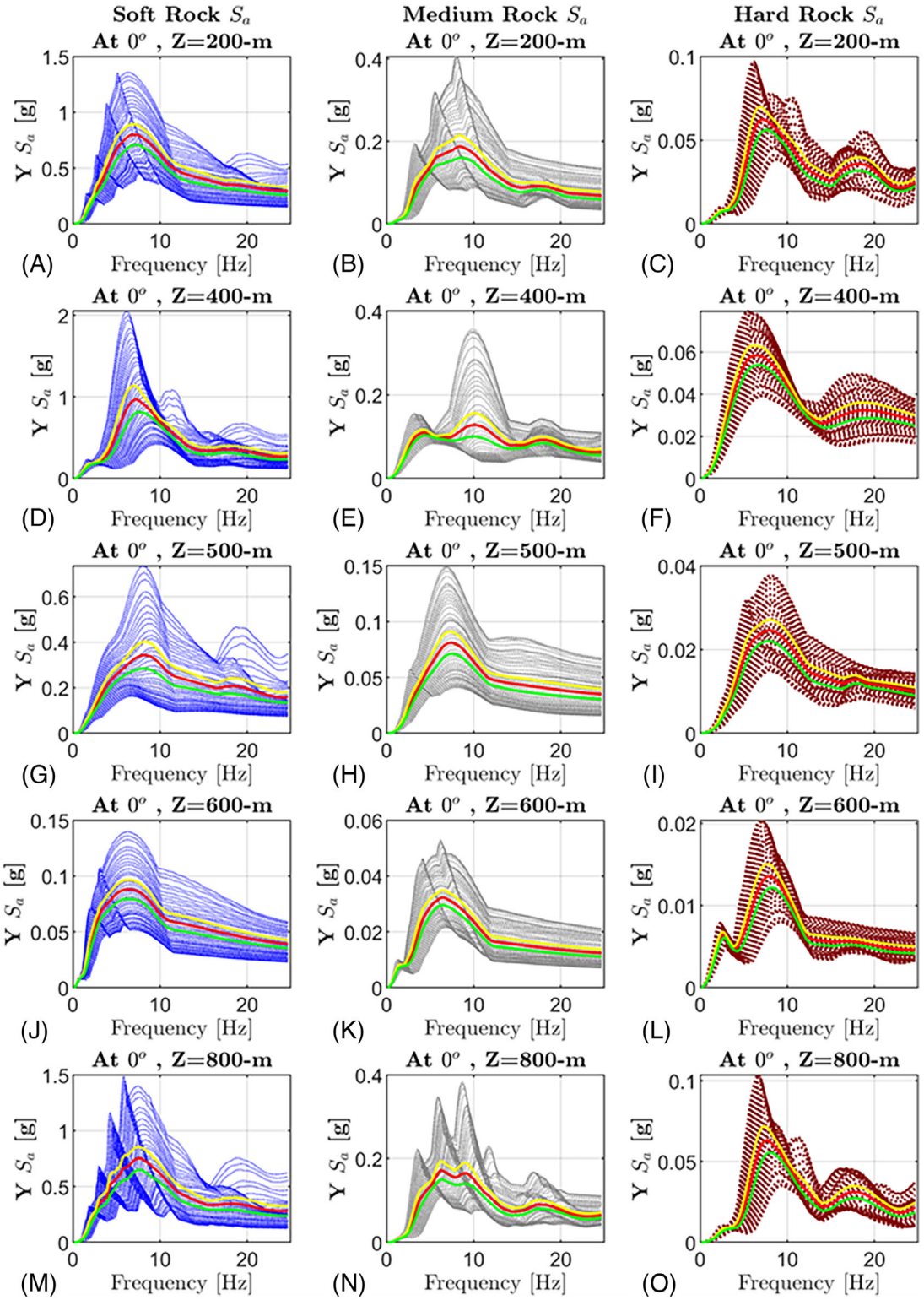


FIGURE 22 Y spectral acceleration spatial variation along the axial direction for different rock media at 0°; i) soft rock (A, D, G, J, M), ii) medium rock (B, E, H, K, N) and iii) hard rock (C, F, I, L, O).

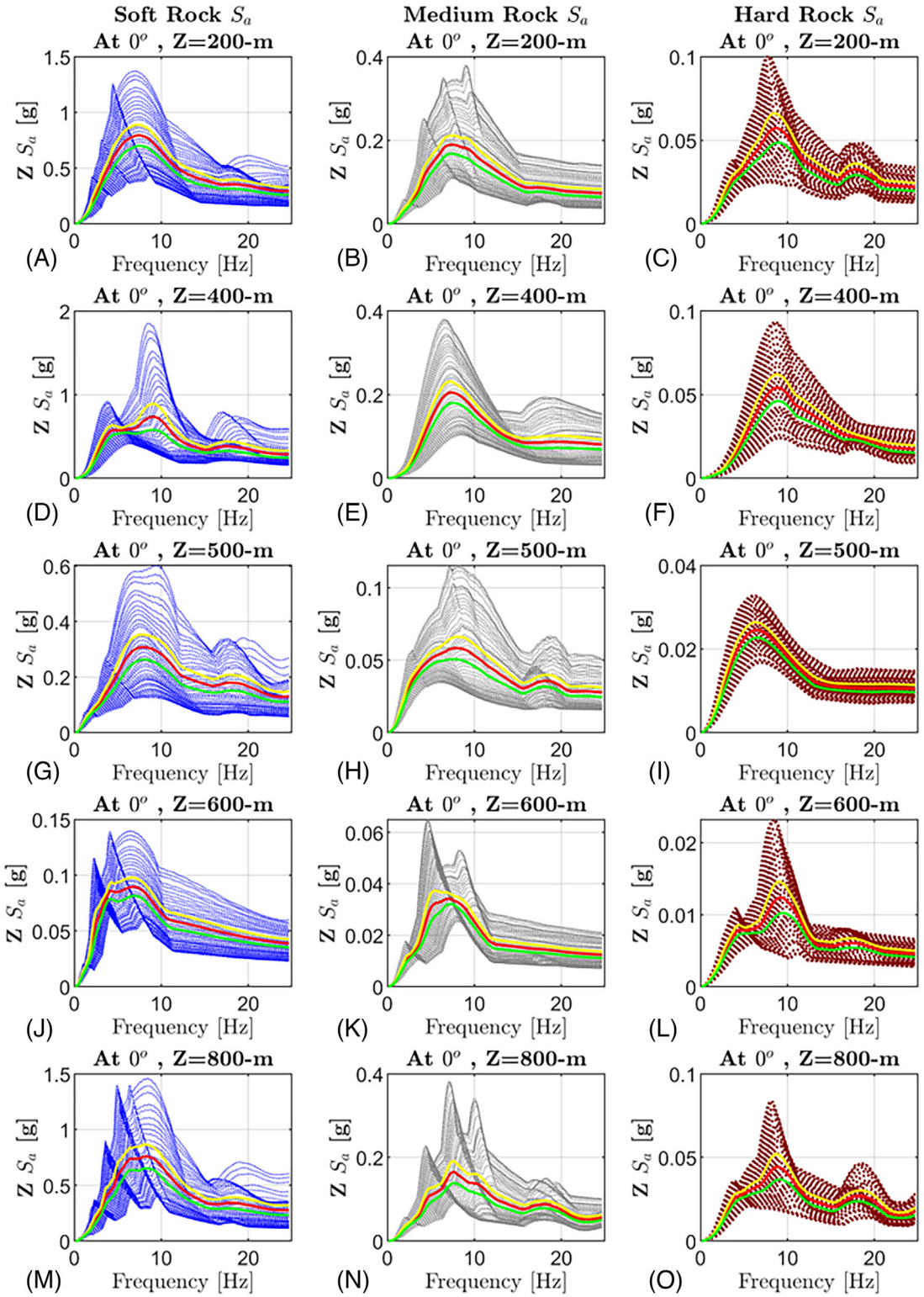


FIGURE 23 Z spectral acceleration spatial variation along the axial direction for different rock media at 0°; i) soft rock (A, D, G, J, M), ii) medium rock (B, E, H, K, N) and iii) hard rock (C, F, I, L, O).

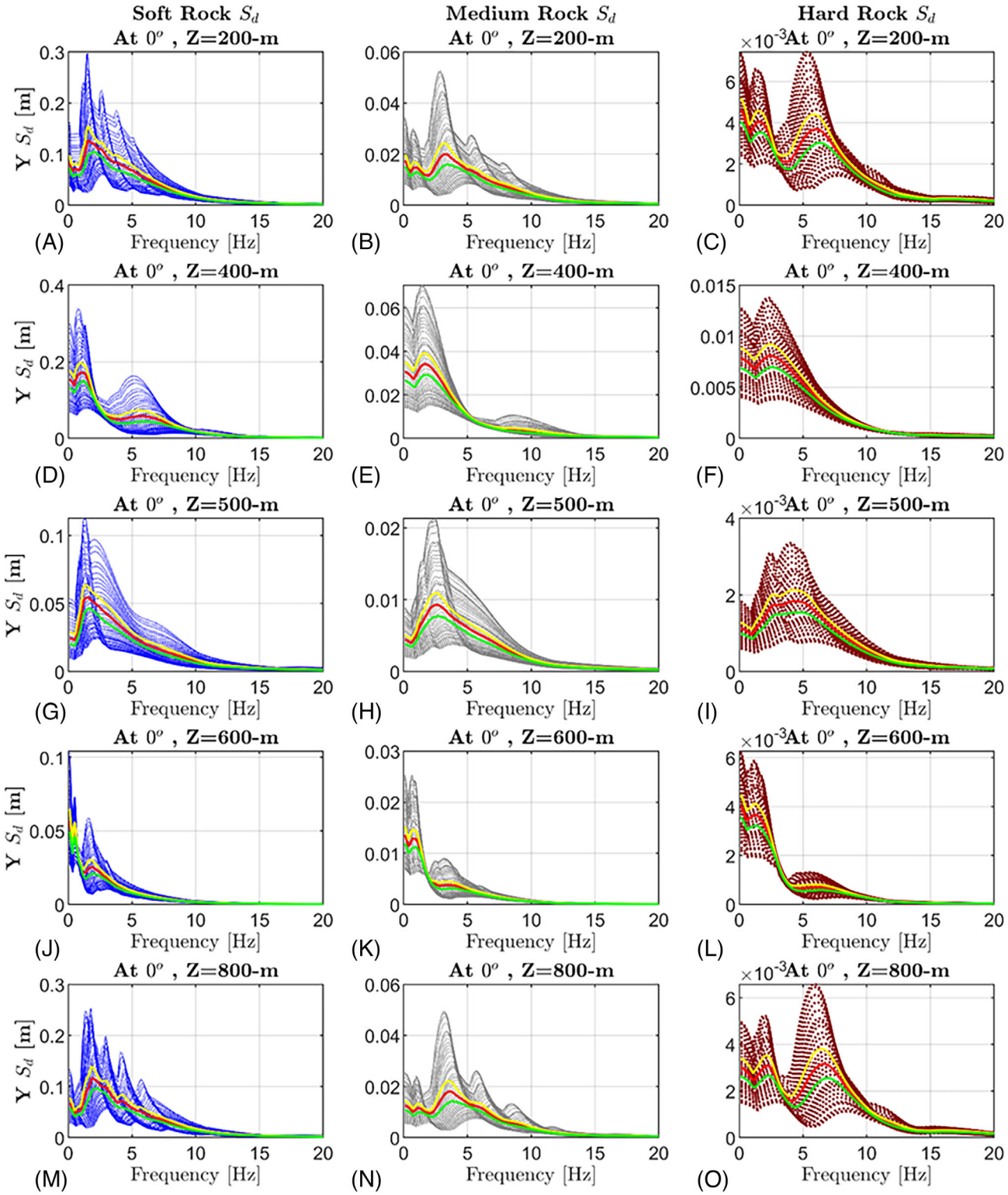


FIGURE 24 Y spectral displacement spatial variation along the axial direction for different rock media at 0°; i) soft rock (A, D, G, J, M), ii) medium rock (B, E, H, K, N) and iii) hard rock (C, F, I, L, O).

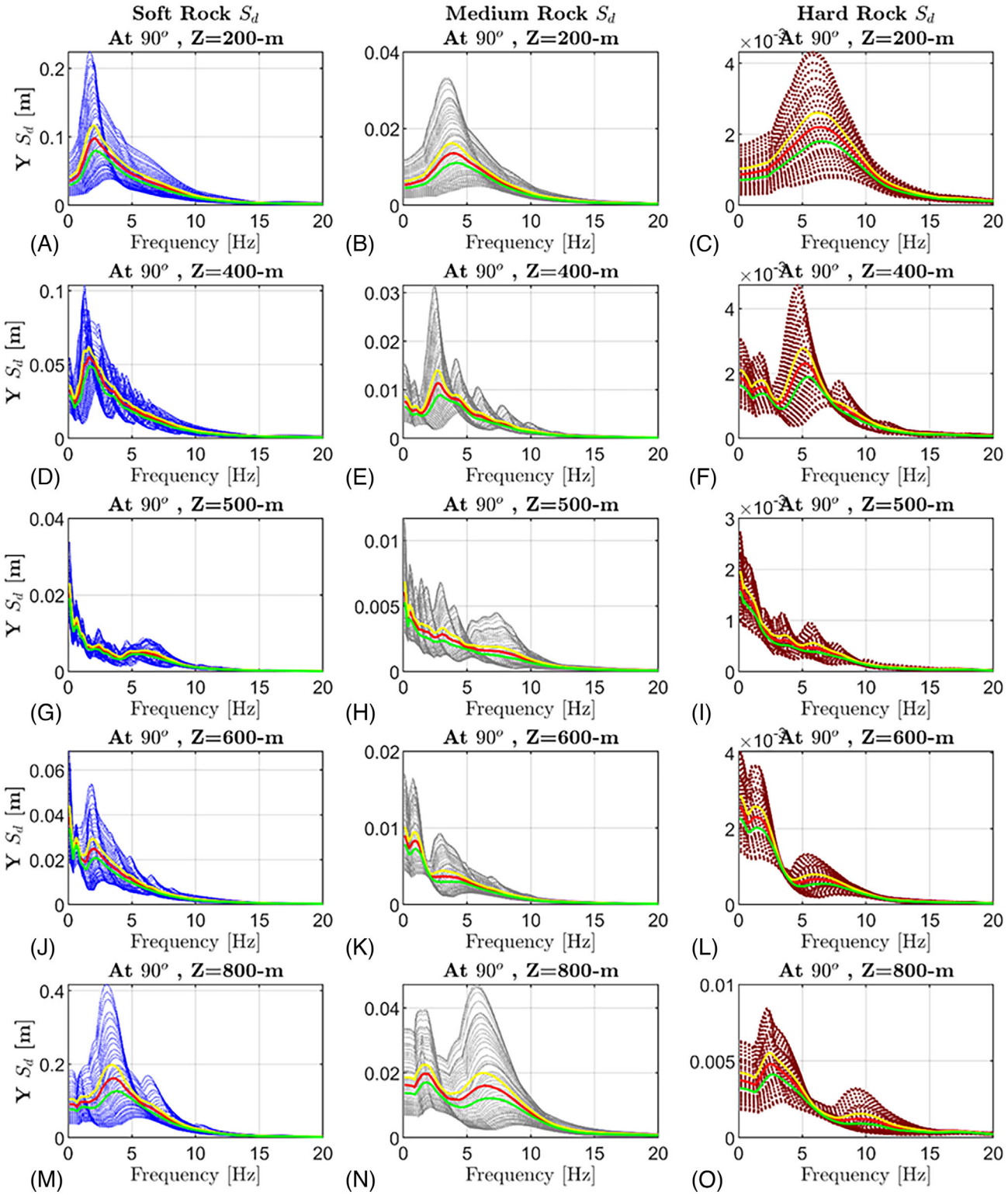


FIGURE 25 Y spectral displacement spatial variation along the axial direction for different rock media at 90°; i) soft rock (A, D, G, J, M), ii) medium rock (B, E, H, K, N) and iii) hard rock (C, F, I, L, O).

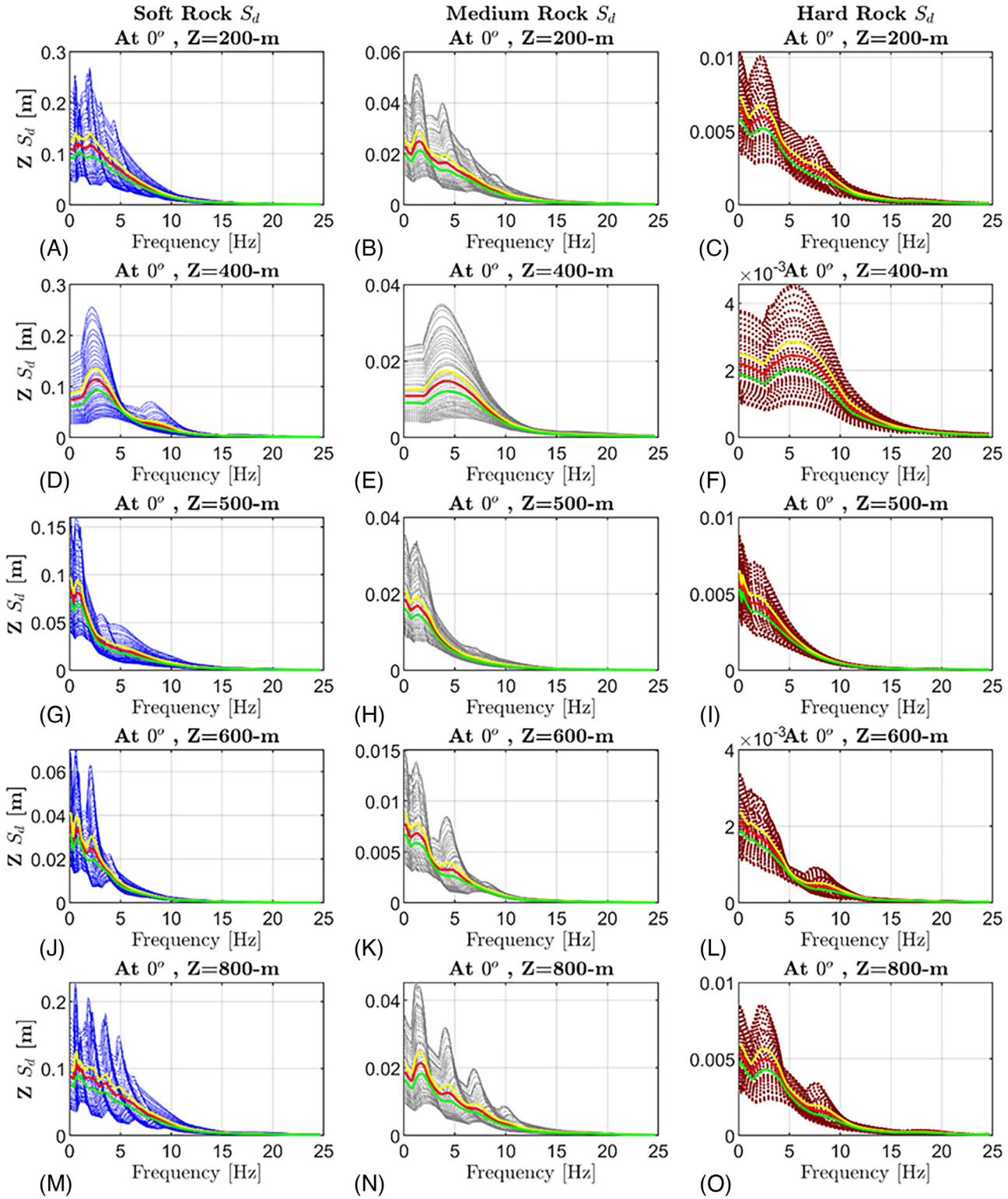


FIGURE 26 Z spectral displacement spatial variation along the axial direction for different rock media at 0°; i) soft rock (A, D, G, J, M), ii) medium rock (B, E, H, K, N) and iii) hard rock (C, F, I, L, O).

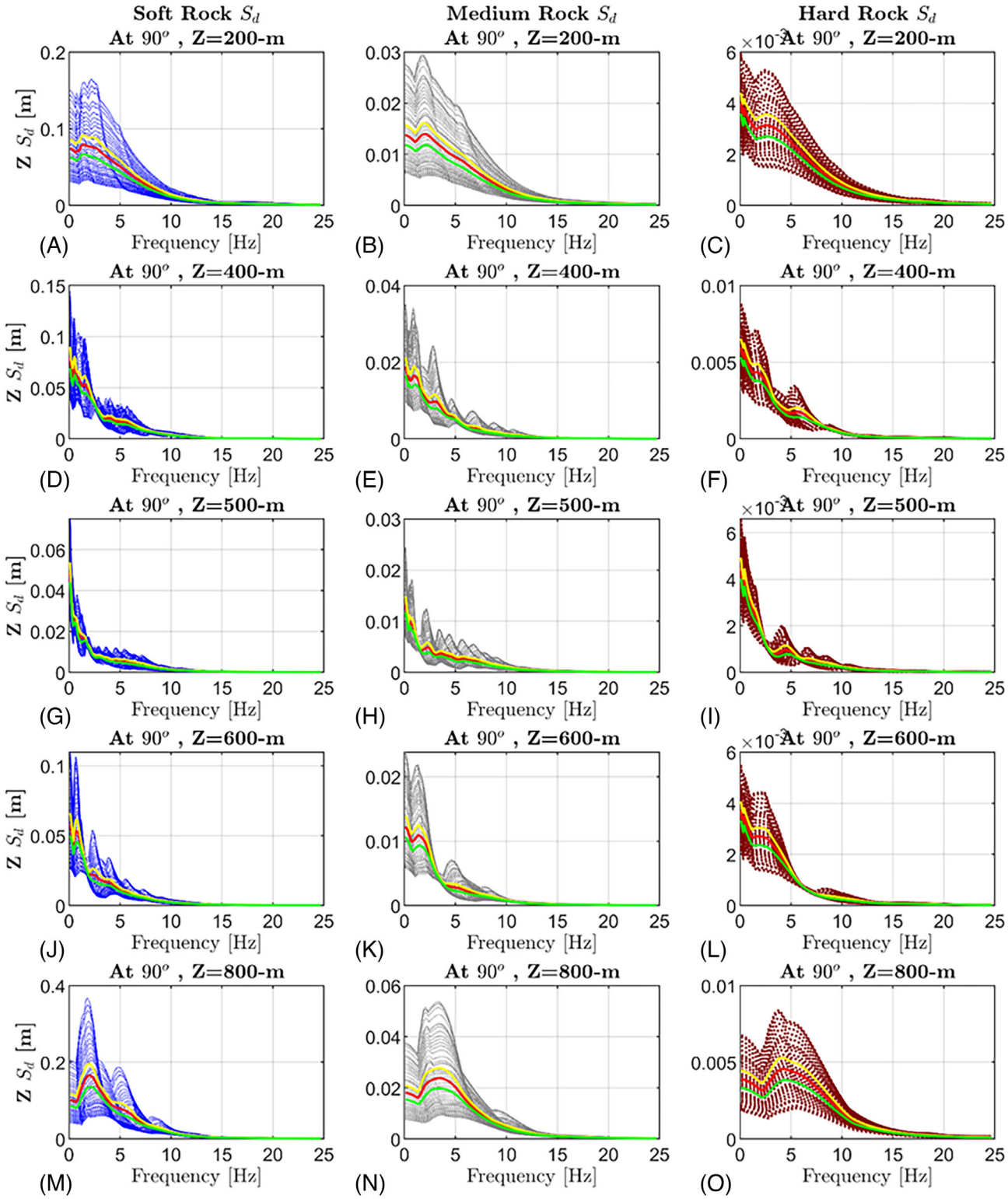


FIGURE 27 Z spectral displacement spatial variation along the axial direction for different rock media at 90°; i) soft rock (A, D, G, J, M), ii) medium rock (B, E, H, K, N) and iii) hard rock (C, F, I, L, O).

structure, generating new frequencies in the domain. The tunnel undergoes ovaling and longitudinal modes of deformation. It was also seen that increase in V_s tends to reduce the intensity of tunnel response. Also, the stiffness of the rock medium plays a role in exacerbating or de-amplifying the response amplitude. The stochastic response spectra plots generated in this study would be beneficial in determining the peak response of tunnels to earthquakes and filtering out the frequencies which are resonant to the tunnel's natural frequency. Appropriate tunnel designs in seismically active regions can be adopted taking into account uncertainties in rock medium properties.

CONFLICT OF INTEREST STATEMENT

The authors declare no conflicts of interest.

DATA AVAILABILITY STATEMENT

Data will be made available on request.

ORCID

Bhavesh Banjare https://orcid.org/0000-0003-2855-0082
Gauri Ranjan Krishna Chand Avatar https://orcid.org/0000-0002-6775-2579

REFERENCES

1. Sharma S, Judd WR. Underground opening damage from earthquakes. *Eng Geol*. 1991;30(3-4):263-276.
2. Jiang Y, Wang C, Zhao X. Damage assessment of tunnels caused by the 2004 Mid Niigata Prefecture Earthquake using Hayashi's quantification theory type II. *Natural hazards*. 2010;53:425-441.
3. Power MS, Rosidi D, Kaneshiro JY. Seismic vulnerability of tunnels and underground structures revisited. *North American Tunneling'98American Underground Construction Association*. 1998.
4. Owen GN, Scholl RE. Earthquake engineering of large underground structures. 2001.
5. Hashash YM, Hook JJ, Schmidt B, John I, Yao C. Seismic design and analysis of underground structures. *Tunn Undergr Space Technol*. 2001;16(4):247-293.
6. Hashash YM, Park D, John I, Yao C. Ovaling deformations of circular tunnels under seismic loading, an update on seismic design and analysis of underground structures. *Tunn Undergr Space Technol*. 2005;20(5):435-441.
7. Penzien J. Seismically induced racking of tunnel linings. *Earthq Eng Struct Dyn*. 2000;29(5):683-691.
8. Ali A, Lyamin AV, Huang J, Sloan SW, Cassidy MJ. Undrained stability of a single circular tunnel in spatially variable soil subjected to surcharge loading. *Comput Geotech*. 2017;84:16-27.
9. Ali A, Lyamin AV, Huang J, Sloan SW, Cassidy MJ. Undrained stability of an unlined square tunnel in spatially random soil. *Geo-Risk 2017*. 2017:507-517.
10. Zhu D, Griffiths DV, Fenton GA. Worst-case spatial correlation length in probabilistic slope stability analysis. *Géotechnique*. 2019;69(1):85-88.
11. Wang MY, Liu Y, Ding YN, Yi BL. Probabilistic stability analyses of multi-stage soil slopes by bivariate random fields and finite element methods. *Comput Geotech*. 2020;122:p.103529.
12. Mollon G, Phoon KK, Dias D, Soubra AH. Validation of a new 2D failure mechanism for the stability analysis of a pressurized tunnel face in a spatially varying sand. *J Eng Mech*. 2011;137(1):8-21.
13. Mollon MG, Phoon KK, Dias D, Soubra AH. Influence of the scale of fluctuation of the friction angle on the face stability of a pressurized tunnel in sands. *Geo-Risk 2011: Risk Assessment and Management*. 2011:225-232.
14. Chong T, Phoon KK, Soubra AH. Stability analysis of a pressurized tunnel face in a spatially varying sand using the statical approach of limit analysis. 2013
15. Eshraghi A, Zare S. Face stability evaluation of a TBM-driven tunnel in heterogeneous soil using a probabilistic approach. *Int J Geomech*. 2015;15(6):p.04014095.
16. Ihlenburg F, Babuška I. Finite element solution of the Helmholtz equation with high wave number Part I: the h-version of the FEM. *Comput Math Appl*. 1995;30(9):9-37.
17. Lysmer J, Kuhlemeyer RL. Finite dynamic model for infinite media. *J Eng Mech*. 1969;95(4):859-877.
18. Basu U, Chopra AK. Perfectly matched layers for transient elastodynamics of unbounded domains. *Int J Numer Methods Eng*. 2004;59(8):1039-1074.
19. Givoli D. Non-reflecting boundary conditions. *J Comput Phys*. 1991;94(1):1-29.
20. Givoli D, Neta B. High-order non-reflecting boundary scheme for time-dependent waves. *J Comput Phys*. 2003;186(1):24-46.
21. Tsynkov SV. Numerical solution of problems on unbounded domains. A review. *Appl Numer Math*. 1998;27(4):465-532.
22. Basu U, Chopra AK. Perfectly matched layers for time-harmonic elastodynamics of unbounded domains: theory and finite-element implementation. *Comput Meth Appl Mech Eng*. 2003;192(11-12):1337-1375.
23. Liao ZP, Wong HL. A transmitting boundary for the numerical simulation of elastic wave propagation. *Int J Soil Dyn Earthquake Eng*. 1984;3(4):174-183.

24. Raghunandan M, Liel AB. Effect of ground motion duration on earthquake-induced structural collapse. *Struct Saf*. 2013;41:119-133.
25. Zafarani H, Noorzad A, Ansari A, Bargi K. Stochastic modeling of Iranian earthquakes and estimation of ground motion for future earthquakes in Greater Tehran. *Soil Dyn Earthquake Eng*. 2009;29(4):722-741.
26. Li Y, Conte JP, Barbato M. Influence of time-varying frequency content in earthquake ground motions on seismic response of linear elastic systems. *Earthq Eng Struct Dyn*. 2016;45(8):1271-1291.
27. Mossessian TK, Dravinski M. Application of a hybrid method for scattering of P, SV, and Rayleigh waves by near-surface irregularities. *Bull Seismol Soc Am*. 1987;77(5):1784-1803.
28. Fäh D, Suhadolc P, Panza GF. A hybrid method for the estimation of ground motion in sedimentary basins: quantitative modeling for Mexico City. *Bull Seismol Soc Am*. 1994;84(2):383-399.
29. Bielak J, MacCamy RC, McGhee DS, Barry A. Unified symmetric BEM-FEM for site effects on ground motion—SH waves. *J Eng Mech*. 1991;117(10):2265-2285.
30. Bielak J, Loukakis K, Hisada Y, Yoshimura C. Domain reduction method for three-dimensional earthquake modeling in localized regions, Part I: theory. *Bull Seismol Soc Am*. 2003;93(2):817-824.
31. Yoshimura C, Bielak J, Hisada Y, Fernández A. Domain reduction method for three-dimensional earthquake modeling in localized regions, part II: verification and applications. *Bull Seismol Soc Am*. 2003;93(2):825-841.
32. Kellezi L. Local transmitting boundaries for transient elastic analysis. *Soil Dyn Earthquake Eng*. 2000;19(7):533-547.
33. Kontoe S, Zdravkovic L, Potts DM. An assessment of the domain reduction method as an advanced boundary condition and some pitfalls in the use of conventional absorbing boundaries. *Int J Numer Anal Methods Geomech*. 2009;33(3):309-330.
34. Kontoe S, Zdravkovic L, Potts DM, Menkiti CO. Case study on seismic tunnel response. *Can Geotech J*. 2008;45(12):1743-1764.
35. Corigliano M, Scandella L, Lai CG, Paolucci R. Seismic analysis of deep tunnels in near fault conditions: a case study in Southern Italy. *Bull Earthquake Eng*. 2011;9:975-995.
36. Kontoe S, Zdravkovic L, Menkiti CO, Potts DM. Seismic response and interaction of complex soil retaining systems. *Comput Geotech*. 2012;39:17-26.
37. Poursartip B, Fathi A, Kallivokas LF. Seismic wave amplification by topographic features: a parametric study. *Soil Dyn Earthquake Eng*. 2017;92:503-527.
38. Graves RW. Simulating seismic wave propagation in 3D elastic media using staggered-grid finite differences. *Bull Seismol Soc Am*. 1996;86(4):1091-1106.
39. Bao H, Bielak J, Ghattas O, et al. Large-scale simulation of elastic wave propagation in heterogeneous media on parallel computers. *Comput Meth Appl Mech Eng*. 1998;152(1-2):85-102.
40. Faccioli E, Maggio F, Paolucci R, Quarteroni A. 2D and 3D elastic wave propagation by a pseudo-spectral domain decomposition method. *J Seismolog*. 1997;1:237-251.
41. Shen Y, Zhong Z, Li L, Du X, El Naggar MH. Seismic response of soil-shield tunnel systems in sandwiched liquefiable soil deposits. *Tunn Undergr Space Technol*. 2023;140:p.105322.
42. Banjare B, Veeraraghavan S, Seismic assessment of tunnels in near fault ground motion. In *Symposium in Earthquake Engineering* (pp. 185-197). Singapore: Springer Nature Singapore. 2022
43. Banjare B. *Seismic evaluation of 3D tunnels in near fault ground motion using domain reduction method*. Indian Institute of Science; 2024. https://etd.iisc.ac.in/handle/2005/6328. M.Sc. thesis.
44. Veeraraghavan S, Bolisetti C, Slaughter A, et al. MASTODON: an open-source software for seismic analysis and risk assessment of critical infrastructure. *Nucl Technol*. 2021;207(7):1073-1095.
45. Lindsay AD, Gaston DR, Permann CJ, et al. 2022. 2.0 - MOOSE: Enabling massively parallel multiphysics simulation. SoftwareX. doi:10.1016/j.softx.2022.101202
46. Newmark NM. A method of computation for structural dynamics. *J Eng Mech*. 1959;85(3):67-94.

How to cite this article: Banjare B, Avatar GRKC. Stochastic assessment of 3-D tunnels in near-fault ground motion using modified domain reduction method. *Int J Numer Anal Methods Geomech*. 2024;48:2259–2284. https://doi.org/10.1002/nag.3733